



Journal of Applied and Computational Mechanics



Research Paper

Geometric Optimization of Jet Pump Used in Vacuum Distillation Applications under Different Operating Conditions using Genetic-algorithm Methods

William Orozco Murillo¹, Iván D. Patiño Arcila², José A. Palacio-Fernández³

¹ Grupo de Investigación e Innovación Ambiental, Facultad de Ingeniería,
I.U. Pascual Bravo. Calle 73 # 73A – 226. 050034 Medellín, Colombia, Email: William.orozco@pascualbravo.edu.co

² Grupo de Investigación e Innovación Ambiental, Facultad de Ingeniería,
I.U. Pascual Bravo. Calle 73 # 73A – 226. 050034 Medellín, Colombia, Email: i.patinoar@pascualbravo.edu.co

³ Grupo de Investigación e Innovación Ambiental, Facultad de Ingeniería,
I.U. Pascual Bravo. Calle 73 # 73A – 226. 050034 Medellín, Colombia, Email: josealpa@pascualbravo.edu.co

Received September 02 2021; Revised November 18 2021; Accepted for publication November 18 2021.

Corresponding author: José Alfredo Palacio Fernandez (josealpa@pascualbravo.edu.co)

© 2022 Published by Shahid Chamran University of Ahvaz

Abstract. Genetic-algorithm methods are used here for single-objective (SO) and multi-objective (MO) geometrical optimizations of jet pumps used in vacuum distillation of ethanol, an application not deeply studied in scientific literature. These devices are particularly suitable to allow the azeotrope-breaking below the atmospheric pressure at ambient temperature. Based on this, different working pressures (P_p), five non-dimensional geometrical parameters that can influence the jet pump operation, and three performance parameters (drag coefficient, pressure recovery ratio and energy efficiency) are considered in this work. Furthermore, using a central composite, face-centered, enhanced experimental design, 89 simulation experiments are run to obtain Response Surfaces (RS) by genetic aggregation, applying afterwards the SOGA and MOGA optimization methods. Also, Spearman Rank-order correlation matrix is employed as initial screening, finding strongly negative correlation of drag coefficient and efficiency with the working pressure, P_p . Computational Fluid Dynamic (CFD) model is validated with other numerical and experimental works, obtaining satisfactory results. Additionally, the change of the optimized input and output parameters with P_p is studied, along with the behavior of Mach number. It can be concluded that the optimal nozzle parameters evidently influenced by P_p for the SO optimization are: outlet diameter and length of divergent part, conicity of convergent part, and ratio of inlet to throat area. For the MO optimization, changes of optimized geometrical parameters with P_p are negligible. In contrast, performance parameters are importantly influenced by P_p for all optimizations.

Keywords: Computational Fluid Dynamics, jet pump performance, geometrical optimization, genetic-algorithm methods, working pressure.

1. Introduction

The principle of a suction jet pump, also known as Venturi pump, is to drive a fluid not involving motion of mechanical parts. The propulsion is provided by the driving jet with a determined flow rate. A primary fluid is forced through a drive nozzle such that an additional flow is generated by internal friction and turbulent mixing at a secondary port [1]. In general, the jet pump efficiencies are significantly lower than efficiencies obtained in centrifugal and positive displacement pumps. However, when costs are taken into account, jet pumps could offer an interesting alternative [2]. Jet pumps can be used in car fuel injection applications [1], weight transport to different ponds [3], dredging systems [4], among others.

Several works have been focused on the jet pump performance assessment. This is the case of Feng et al. [5], where it was found that the geometry of the primary nozzle of ejectors used for recirculation of hydrogen in proton exchange membrane fuel cell (PEMFC) systems, has relevant effects on the ejector performance. Another case is the one of El-Sawaf et al. [6], where they found that a diffuser angle of $\theta_d=5.5^\circ$ leads to higher efficiencies than the other two angles considered, $\theta_d=4^\circ$ and $\theta_d=7^\circ$. Additionally, it was found that for a given area ratio, as defined by the ratio of nozzle area to mixing chamber area, and a diffuser angle of $\theta_d=7^\circ$, the losses due to separation increase, whereas for a diffuser angle of $\theta_d=4^\circ$, the diffuser length increases and consequently, friction loss increases as well.

The geometry of the primary nozzle plays a key role in the jet pump performance. In this sense, ejectors include the subsonic ejectors and the supersonic ejectors, which have a convergent nozzle and a convergent-divergent nozzle, respectively, as shown in Figure 1. Thus, when divergent angle, α_{nd} , equals zero, the supersonic nozzle becomes subsonic. Besides, in [5], four geometric



parameters of the nozzle geometry were studied, namely, throat diameter (D_t), convergent angle (α_{nc}), divergent angle (α_{nd}), and divergent length (L_{nd}), finding that supersonic ejectors could have better performance than subsonic ones under critical conditions. In a similar fashion, Zhu and Jiang [7] found that, for the same experimental conditions, the first shock length of supersonic nozzles is significantly larger than such of the subsonic ones; for the entrainment ratio, higher values were obtained in supersonic ejectors. Nevertheless, in some special applications, such as the refrigeration systems using solar energy as power source, a better performance has been reported for subsonic nozzles [8]

Thongtip and Aphornratana [9] investigated the primary nozzle geometry for refrigeration systems; and their results showed that the primary nozzle should be carefully designed according to the operating conditions. Also, In Rao and Jagadeesh [10], two novel supersonic nozzles that introduce changes in the nozzle outlet were developed: tip ring supersonic nozzle and shallow pointed elliptical lobed nozzle. These nozzle geometries improved the mixing in supersonic jets with minimum pressure loss due to fluid stagnation. On the other hand, Wang et al. [11] performed a simulation analysis on the geometric parameters of the primary nozzle in ejectors used in refrigeration systems, where it was found that the angle and length of the divergent zone have significant effects on the ejector performance. Furthermore, the study of Hakkaki-Fard [12] showed that the nozzle outlet diameter could affect the ejector performance; and, for PEMFC systems, both supersonic [13, 14] and subsonic nozzles [15, 7] have been deemed. Some authors have found a better entrainment performance for supersonic ejectors, but this finding is still controversial. Finally, considering the aforementioned works, it is interesting to study the effects of the primary nozzle geometry on the ejector performance.

In 2013, William Orozco [16-18], co-author of the present work, developed a unidirectional analytical model to obtain the optimum geometry and dimensions of a jet pump used in vacuum distillation of ethanol. By using pressures below 101.3 kPa and temperatures below 78.6 °C, ethanol azeotrope can break and distillation can occur to obtain mixing purities higher than 95/5% ethanol / water [19]. Figure 2b shows the industrial scheme of the implementation of a jet pump in vacuum distillation systems. Similarly, the model developed in [16, 17] allows finding, among other parameters, the ideal diameter of the nozzle throat to generate a vacuum pressure of 8 kPa in the secondary fluid, for certain conditions of pressure and mass flow rate of the primary fluid, and keeping the drag coefficient close to $C_d=0.5$. The theoretical behavior of the fluid flow along the jet pump, in terms of the pressure and Mach number, when pump is operating in normal conditions, can be observed in Figure 2a. Recently, William Orozco et al [18] published a work focused on performing CFD simulations of jet pumps used in the vacuum distillation of ethanol, using the standard $k-\epsilon$ turbulence model and the classical mass and energy conservation equations. In such a work, a parametric analysis about the influence of the primary (inlet) fluid pressure and the location of the primary nozzle regarding the secondary one, in the jet pump performance was carried out. In addition, the pump performance was studied in terms of the drag coefficient and the behavior of the mach number and total pressure over the fluid domain.

This research deals with the geometrical optimization of jet pumps used in vacuum distillation of ethanol, which is relevant in order to obtain the better performance of these devices when distillation process occurs at 8 kPa and ambient temperature, reducing the energy consumption with respect to a classical distillation process at atmospheric pressure and 78.6 °C. As abovementioned, most of the works focused on jet pump optimization consider dimensional geometrical parameters (diameter of nozzle inlet, nozzle throat and nozzle outlet, length of convergent and divergent part of nozzle, length of mixing chamber, among others). In the present work, a geometrical optimization of a jet pump used for vacuum distillation of ethanol is done considering five non-dimensional input parameters that relate important dimensions of the jet pump, harnessing the advantages of the non-dimensionalization: reduction of experiments, independency of the units of measurement, scale prototyping, better insight of significant and non-significant parameters, among others. Dimensions used to build the non-dimensional parameters are shown in blue color in Figure 3 and they are referred to as: diameter of nozzle inlet (D_1), diameter of nozzle throat (D_g), diameter of nozzle outlet (D_2), length of divergent part of diffuser (L_{div}), diameter of straight part of diffuser (D_c), length of mixing chamber (L_{mix}) and length of convergent part of the nozzle (L_{conv}). The non-dimensional geometrical parameters are described in Section 3.

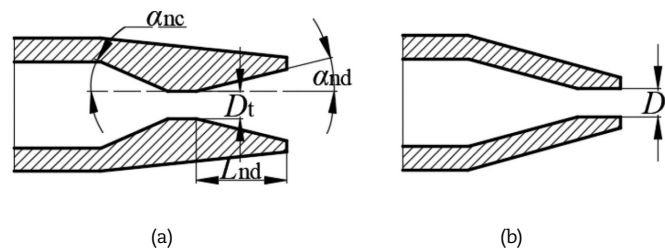


Fig. 1. (a) Supersonic nozzle, (b) Subsonic nozzle [5].

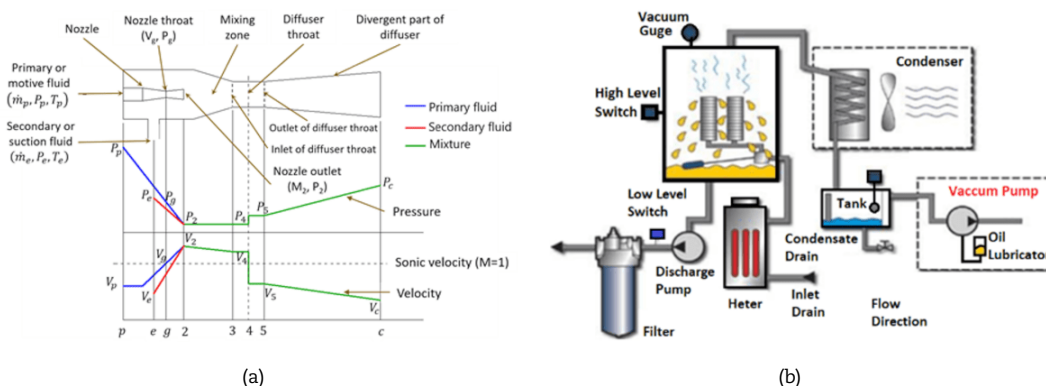


Fig. 2. a) Scheme of basic parts and field variables behavior of jet pump [16, 17], b) Industrial scheme of the use of a jet pump in vacuum distillation systems [19]



In this work, both single-objective (SO) and multi-objective (MO) geometrical optimizations are carried out, using the Response Surface Optimization Methodology. In the SO optimizations, the drag coefficient (C_d), pressure recovery ratio (PR) and energy efficiency (η) are independently optimized by means of Single-Objective Genetic Aggregation (SOGA), whereas in the second case, a MO optimization considering the three parameters is performed using Multi-Objective Genetic Aggregation (MOGA). Likewise, genetic-algorithms methods have been widely used in different physics. For instance, for heat transfer problems, three recent works can be found in [20-22]. In Bianco et al. [20], multi-objective Pareto optimization of finned heat sinks with phase change materials and metal foams was performed using a genetic algorithm. This work was focused on minimizing the cost of these devices, while maximizing the operation time. The maximization of heat rate and minimization of pumping power in non-finned and finned metal foam heat sinks, was carried out by Bianco et al. [21] using genetic algorithms developed in MATLAB, calibrating the closing coefficients of governing equations by means of experiments, and modifying morphological, geometrical and fluid-dynamic parameters. In a similar fashion, Li et al. [22] used variance analysis, surrogate models and non-dominated sorting genetic algorithms to optimize the power density, system efficiency and oxygen distribution uniformity on proton exchange membrane fuel cell (PEMFC), obtaining satisfactory results regarding the base model, with an important reduction in the computational cost.

The present work is organized as follows: In Section 2, the parametric CFD model is described, including the geometrical modeling, fluid definition, mesh definition and analysis, governing equations and numerical setup, and boundary conditions. Then, in Section 3, the non-dimensional input and output parameters are presented, as well as the kind of Design of Experiment (DOE) used to generate the design points, and the optimization methodology employed. Subsequently, results and discussion are tackled in Section 4. In this section, the computational model considered for the CFD simulations is validated with experimental and other numerical results previously published [5]. Additionally, DOE results for the CFD simulations are presented, a correlation analysis is done using the Spearman Rank-Order correlation matrix and local sensitivity analysis is carried out as well, to depict an initial screening about the influence of the non-dimensional input parameters on the three performance parameters of the jet pump (C_d , PR and η). Afterwards, the change of the optimum non-dimensional geometrical parameters obtained from the single-objective (SO) and multi-objective (MO) optimizations, with the primary (inlet) pressure, P_p , is analyzed. The behavior of the performance parameters of the jet pump (C_d , PR and η), with the non-dimensional geometrical parameters for the multi-objective optimization (MO) and of the Mach number in the fluid domain for some optimized geometries, are studied as well in this section. Lastly, in Section 5, conclusions of the present work are presented.

2. Computational Fluid Dynamics Analysis

2.1 Geometrical modeling and fluid definition

The modeling of the fluid domain was carried out in the software Design Modeler™, and the non-dimensional parameterization was defined as evidenced later in Section 3. As shown in Figure 4a, a half domain is formed by revolving 180° a parametric sketch. A sample dimensioned sketch is shown in Figure 4b. Figure 4a,b obviates some constructive details of the jet pump without affecting the numerical analysis. In fact, some authors have used 2D axisymmetric simplification to simulate the fluid flow in jet pumps [15, 23, 24], which entails an important reduction in the computational cost. However, the implications of this simplification have been discussed in several works, finding noticeable differences with 3D CFD results and experiments for some situations. For instance, several authors agree that the arising of 3D vortical structures in turbulent flows, which are not captured in 2D axisymmetric analyses, have an important influence on the fluid flow behavior for subcritical conditions [5, 25, 26]. These conditions can be reached in some points along the longitudinal direction of the jet pump (see Figure 2a). Shah, Chughthai and Inayat [27] considered 3D CFD analysis as the best choice to simulate the thermal hydrodynamic phenomena in steam jet pumps, when using a two-phase Eulerian model together with a direct contact condensation model. Similarly, Song et al. [28] employed a 3D model to simulate the erosion phenomenon in a jet pump under different working conditions by using the Finnie’s model, where the influence on the mass flow ratio, pressure ratio and efficiency was evaluated. In order to reproduce better the turbulent structures, Yapici and Aldas [29] considered a 3D computational model for the maximization of the energy efficiency of water jet pumps in terms of the area ratio, nozzle position and length of mixing chamber.

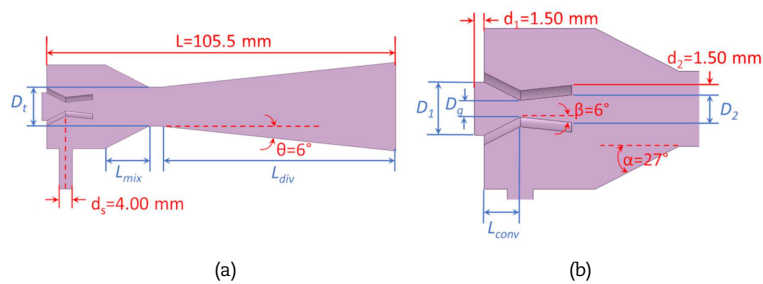


Fig. 3. Dimensions of the jet pump considered in the present work. (a) All domain, b) Detail of nozzle. In red color, they are shown the fixed dimensions, whereas varying dimensions are represented in blue color.

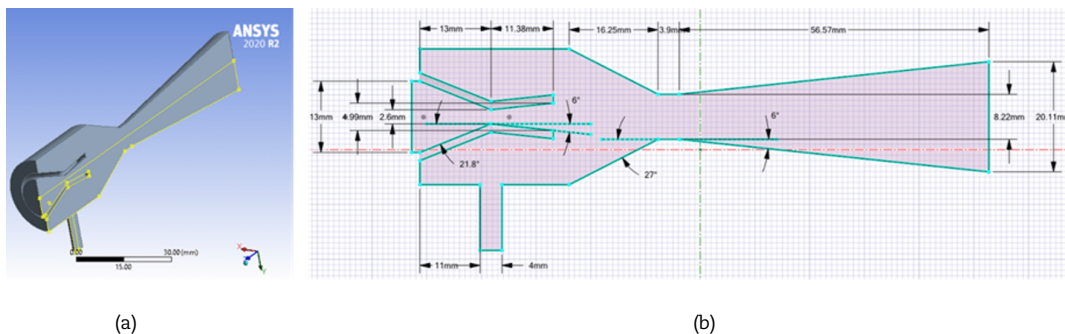


Fig. 4. a) Geometric generation of the jet pump, b) Dimensions of the sketch for a determined case.



Table 1. Relative errors and increment of the computation time with the change of the global mesh size.

Change of the global mesh size	Relative error for drag coefficient	Relative error for pressure recovery ratio	Relative error for energy efficiency	Relative increment of computation time (min)
1 to 0.8 mm	14.3%	26.3%	14.4%	50%
0.8 to 0.6 mm	10.0%	17.9%	9.3%	70%
0.6 to 0.4 mm	7.4%	13.0%	9.1%	140%
0.4 to 0.3 mm	0.4%	1.0%	1.1%	110%
0.3 to 0.2 mm	0.2%	0.5%	0.3%	190%

Computational fluid dynamics (CFD) simulations were carried out in ANSYS Fluent™, where a compressible air domain governed by the ideal gas law was considered, involving properties given as: specific heat of $C_p=1006.43 \text{ J/kgK}$, thermal conductivity of $K=0.0242 \text{ W/mK}$, viscosity of $\mu=1.79E-05 \text{ kg/ms}$, molecular weight of 28.96 g/mol . In the present work, as in the ones published in [16-18], species transport phenomenon is not simulated (ethanol + air + water mixture), but it is deemed an air domain with secondary pressure held at 8 kPa to allow ethanol distillation.

2.2 Mesh definition, mesh quality and mesh dependence analysis

The types of elements used for the fluid domain are linear tetrahedral and linear wedge (Tet4 and Wed6), with a global mesh size of 0.4 mm , local mesh refinement of 0.2 mm in the nozzle walls, and mesh inflation in the nozzle walls with transition ratio of 0.6 and growth rate of 1.1 , as can be seen in Fig. 5a, b. The characteristics of this mesh were obtained after performing convergence analyses for several jet pump geometries; for the particular geometry shown in Figure 4b, convergence analysis can be appreciated in Figure 6, where the drag coefficient (C_d), pressure recovery ratio (PR) and energy efficiency (η), as well as the computation time, are shown in terms of the number of nodes of each mesh. As a result, all meshes were generated with the same controls previously mentioned, maintaining constant the ratio between the global and local mesh size by two. As can be observed, six meshes were considered, with the following global sizes and number of nodes: 1 mm (51141 nodes), 0.8 mm (81348 nodes), 0.6 mm (147504 nodes), 0.4 mm (360110 nodes), 0.3 mm (652693 nodes) and 0.2 mm (1585785 nodes). In curves of Figure 6, the markers corresponding to the selected mesh (global size of 0.4 mm) are colour-filled. As can be observed, any mesh refinement from this selected mesh does not entail a significant change of the performance parameters (C_d , PR or η), but a considerable increase of the computation time. This can be confirmed in Table 1, where the relative errors, E, and the relative increment of the computation time for each change of mesh size, are shown. In such case, the relative error is computed as follows:

$$E = \left\| \frac{P^{(2)} - P^{(1)}}{P^{(1)}} \right\| \tag{1}$$

where $P^{(2)}$ and $P^{(1)}$ represent the performance parameter (C_d , PR or η) corresponding to two subsequent mesh configurations represented by 2 (finer mesh) and 1 (rougher mesh), respectively. In Table 1, It is worth-noticeable, for example, that an increase from the selected mesh (0.4 mm , 360110 nodes) to the immediately superior mesh (0.3 mm , 652693 nodes) generates a variation in C_d , PR and η of 0.4% , 1.0% and 1.1% , respectively, at the expense of an increment in the computation time of 110% , indicating that this mesh refinement is not practical. In the present work, numerical simulations were executed in a computer with processor Intel(R) Xeon(R) E-2286M, 2.4 GHz , 64 GB RAM .

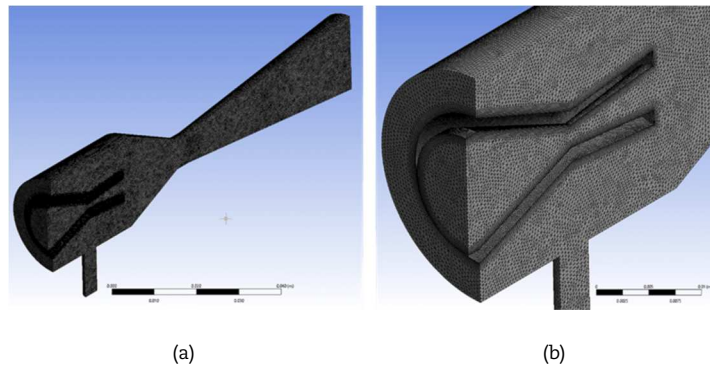


Fig. 5. Mesh of the jet pump. a) Global view, b) Detailed view of the inflation zone.

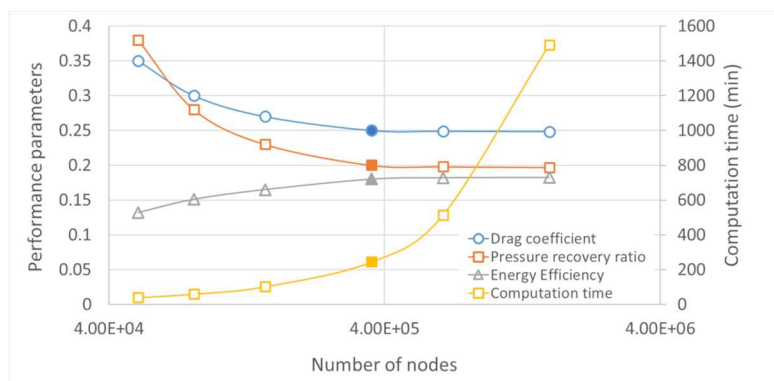


Fig. 6. Performance parameters (C_d , PR, η) and computation time in terms of the number of nodes, highlighting the points of the selected mesh.



Table 2. Assessment of element quality according to the skewness.

Skewness Value	Element Classification
0	Ideal
>0-0.25	Excellent
0.25-0.5	Good
0.5-0.75	Moderate
0.75-0.9	Moderate to bad
0.9-<1	Bad
1	Degenerate

Mesh Skewness is used in the present work as mesh quality metric. Skewness of zero indicates that element is ideal, while a skewness of one means that all nodes of the element are coplanar. Table 2 shows the classification of element quality according to their skewness. For tetrahedral elements, skewness is:

$$\text{Skewness} = (V_{opt} - V_{real}) / V_{opt} \tag{2}$$

where V_{real} is the volume of the real element, while V_{opt} is the optimal volume, defined as the volume of an ideal element with the same circumradius as the real element. As can be seen in Figure 7, most of the elements have excellent, good or moderate quality.

2.3 Governing equations and numerical setup

Reynolds-averaged Navier-Stokes (RANS) approach is employed for the CFD simulations. Specifically, the k-ε turbulence model, which has been previously used for fluid-dynamic simulations of jet pumps [18, 30-34], is used. Governing equations are given by [35, 36]:

- Mass conservation:

$$\frac{\partial \rho}{\partial t} + \nabla \cdot (\rho \vec{v}) = S_m \tag{3}$$

where ρ , \vec{v} and S_m , represent density, velocity vector and interphase mass transfer (zero in this case), respectively.

- Momentum and k-ε equations: In addition to the Reynolds-averaged Navier-Stokes equations, two additional equations are considered for k and ε.

$$\frac{\partial}{\partial t}(\rho k) + \frac{\partial}{\partial x_i}(\rho k u_i) = \frac{\partial}{\partial x_j} \left[\left(\mu + \frac{\mu_t}{\sigma_k} \right) \frac{\partial k}{\partial x_j} \right] + G_k + G_b - \rho \varepsilon - Y_M + S_k \tag{4}$$

$$\frac{\partial}{\partial t}(\rho \varepsilon) + \frac{\partial}{\partial x_i}(\rho \varepsilon u_i) = \frac{\partial}{\partial x_j} \left[\left(\mu + \frac{\mu_t}{\sigma_\varepsilon} \right) \frac{\partial \varepsilon}{\partial x_j} \right] + C_{1\varepsilon} \frac{\varepsilon}{k} + (G_k + C_{3\varepsilon} G_b) - C_{2\varepsilon} \rho \frac{\varepsilon^2}{k} + S_\varepsilon \tag{5}$$

where k and ε are the turbulent kinetic energy and dissipation rate, respectively; G_k and G_b are generation terms of turbulence kinetic energy associated to the average velocity gradients and buoyancy, respectively, as given by $G_k = \mu_t S^2$ and $G_b = \beta g_i (\mu_t / Pr_t) \partial T / \partial x_i$, with S as the mean strain rate tensor, β as the coefficient of thermal expansion and Pr_t as the energy Prandtl number. The density and velocity field are represented by ρ and u_i , whereas μ_t is the turbulent viscosity, as computed by:

$$\mu_t = \rho C_\mu (k^2 / \varepsilon) \tag{6}$$

Contribution of fluctuating dilatation to the overall dissipation rate is represented by Y_M , which shall be activated for supersonic flows, selecting the compressibility correction of ANSYS Fluent™. This term is computed as $Y_M = 2\rho\varepsilon(Ma)^2$, with Ma as the Mach number. Constants of the k-ε turbulence model are summarized in Table 3.

- Energy equation:

$$\frac{\partial(\rho E)}{\partial t} + \nabla \cdot (\vec{v}(\rho E + P)) = \nabla \cdot [K_{eff} \nabla T - \sum_j h_j \vec{J}_j + (\vec{\tau}_{eff} \cdot \vec{v})] + S_h \tag{7}$$

where E, P, K_{eff} , h_j , \vec{J}_j , $\vec{\tau}_{eff} \cdot \vec{v}$ and S_h are total energy, pressure, effective thermal conductivity, enthalpy, diffusive flux of species (zero in this case), dissipation viscous term and source term, respectively.

To relate the solution variables in the cells adjacent to walls with the corresponding variables of the walls, the Enhanced Wall Treatment method is considered, where enhanced wall functions and two-layer modelling are combined to estimate the fluid flow quantities in the boundary layer with coarser meshes rather than classical near-wall approaches, lowering the computational cost. In order to guarantee the location of the first cell in the log-layer, it is advisable to maintain the dimensionless wall distance of this cell, y^+ , in between 30 and 300. For the inflation mesh represented in Figure 5, y^+ for the first cell ranges between 62 and 85 in all simulations considered here, fulfilling this recommendation; additionally, growth rate (1.1), transition ratio (0.6) and number of layers (10) allow a smooth transition between the wedge-type inflation mesh and the tetrahedral one.



Table 3. Constants of the k-ε turbulence model

Constant symbol	Value
C_{μ}	0.09
$C_{1\varepsilon}$	1.44
$C_{2\varepsilon}$	1.92
σ_k	1.0
σ_ε	1.3
Pr_t	0.85

Table 4. Summary of boundary conditions

Region	Type	Value/Characteristics
Primary port	Gauge pressure	10-100 kPa
Secondary port	Absolute pressure	8 kPa
Outlet port	Initial gauge pressure	4.5 kPa
Longitudinal plane	Symmetry condition	Non-flux, Zero shear stress
External walls	Wall condition	No penetration, no slip, stationary
Internal walls	Wall condition	No penetration, no slip, stationary

On the other hand, the reference values used in the computation of the derived physical quantities, dimensionless coefficients in the postprocessing stage, initialization, solution scheme, spatial discretization, gradient calculation and relaxation factors are configured as in [18]. Moreover, the classical convergence monitors and their respective allowable residuals are: Continuity (1E-06); Velocity-X (1E-06); Velocity-Y (1E-06); Velocity-Z (1E-06); Energy (1E-06); K parameter (1E-06); ε parameter (1E-06). Additionally, the three performance parameters considered in the present work are configured as convergence monitors, as follows: Drag coefficient, C_d (1E-06), Pressure Recovery Ratio, PR (1E-06) and Energy Efficiency, η (1E-06).

2.4 Boundary conditions

Boundary conditions are prescribed at the domain faces as shown in Figure 8. Besides, symmetry condition is considered in the longitudinal plane of the pump. Also, at the inlet of primary fluid, a parametric gauge pressure condition is assigned, ranging between 10 kPa and 100 kPa. These primary pressures have same orders of magnitude as the ones considered in previous numerical and experimental works: Orozco et al. [16-18], Varga et al. [37], Rusly et al. [38], Huang and Chang [40]. In such inlet port, air temperature of 298 K is prescribed. Additionally, the option “Prevent reverse flow” is activated to avoid backflows during iterations that can disrupt the numerical solution. In such boundary, turbulence intensity is set in 5% and hydraulic diameter matches the nozzle inlet diameter. On the other hand, an absolute pressure of 8 kPa is assigned at the secondary port, because this is the pressure to azeotropically distill ethanol at ambient temperature. This way, air temperature of secondary fluid is considered as 295 K, “Prevent reverse flow” control is activated as well, turbulence intensity value of 5% is considered and the diameter of the secondary port is deemed as the hydraulic diameter. Furthermore, over the face corresponding to diffuser outlet, initial pressure condition of 4.5 kPa, temperature of 295K, turbulence intensity of 5% and hydraulic diameter equal to the diffuser outlet one are assigned, but these conditions are modified as simulation is executed. Finally, a wall-type condition (not slip and zero penetration) is prescribed over the remaining faces of the domain. The boundary conditions are summarized in Table 4.

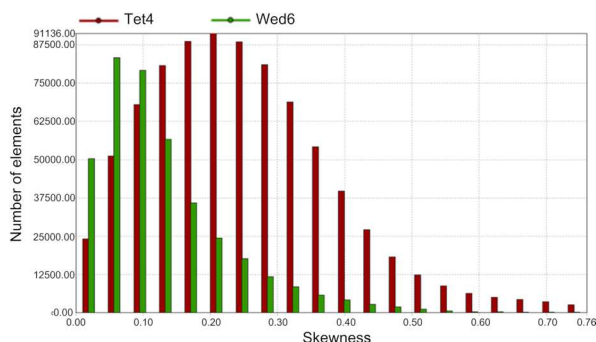


Fig. 7. Skewness distributions of mesh elements.

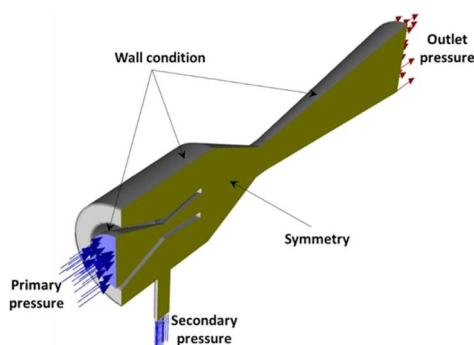


Fig. 8. Boundary conditions of CFD simulations.



3. Design of Simulation Experiments and Optimization Techniques

As mentioned above, input parameters considered in the present work are non-dimensional. In this sense, in specialized literature about jet pumps [37-42], some relationships between geometrical dimensions that can be significantly influential on the jet pump performance have been reported. In Figure 3, the geometrical dimensions involved in the definition of the non-dimensional parameters are shown in blue. In the present work, the following non-dimensional input parameters are considered:

- Parameter λ : This parameter is used to range the diameter of the nozzle outlet (D_2) between such of the nozzle throat (D_g) and the one of nozzle inlet (D_1), according to equation (8). In the present work, this parameter changes between $\lambda = 0.01$ and $\lambda = 0.3$. The diameter of the nozzle throat is set to 2.6 mm for all simulations.

$$D_2 = D_g(1 - \lambda) + D_1\lambda \quad (8)$$

- Parameter R_d : This is defined as the ratio between the length of divergent part of the diffuser (L_{div}) and diameter of the straight part of the diffuser (D_t), equation (9), ranging between 5 and 7.5 in the present work.

$$R_d = L_{div}/D_t \quad (9)$$

- Parameter X: This is defined as the ratio between the length of the mixing chamber (L_{mix}) and the diameter of the nozzle throat (D_g), equation (10), varying between 4 and 7 in the present work.

$$X = L_{mix}/D_g \quad (10)$$

- Parameter L_{1g} : Ratio between the length of convergent part of the nozzle (L_{conv}) and half difference between diameters of inlet and throat nozzle, equation (11), changing between 1 and 3 in the present work. The lower L_{1g} , the higher the conicity angle of convergent part of nozzle.

$$L_{1g} = \frac{L_{conv}}{(D_1 - D_g)/2} \quad (11)$$

- Parameter RA: Ratio between the areas of the inlet (A_1) and throat (A_g) of the nozzle, equation (12) to (14), varying between 10 and 30 in the present work.

$$RA = A_1/A_g \quad (12)$$

$$A_1 = \pi D_1^2/4 \quad (13)$$

$$A_g = \pi D_g^2/4 \quad (14)$$

In Figure 3, other fixed dimensions required to define the jet pump geometry, namely, diameter of secondary port (d_s), distance between nozzle inlet and rear interior wall (d_1), thickness of nozzle wall (d_2), cone half-angle of divergent part of nozzle (β), cone half-angle of mixing chamber (α), cone half-angle of divergent part of diffuser (θ) and total length of the jet pump (L) are shown in red color. On the other hand, the only changeable processing parameter considered here is the primary or inlet gauge pressure (P_p), which ranges between 10 kPa and 100 kPa.

In the present work, three performance parameters are considered as objective variables of optimization, namely, drag coefficient (C_d), pressure recovery ratio (PR) and energy efficiency (η). These parameters have been previously used in scientific literature [37-42] and can be defined as follows:

- Drag coefficient: this parameter is extensively used to account for the jet pump performance. It is defined as the ratio of the mass flow rate at the secondary port, \dot{m}_s , to the mass flow rate as the primary one, \dot{m}_p , as given by equation (15).

$$C_d = \dot{m}_s/\dot{m}_p \quad (15)$$

- Pressure recovery ratio: this parameter accounts for the pressure recovery from the secondary (suction) to the outlet (discharge) port (P_d - P_s) with respect to the global pressure gradient between the primary (inlet) and outlet (discharge) port (P_p - P_d), as shown in equation (16).

$$PR = (P_d - P_s)/(P_p - P_d) \quad (16)$$

- Energy efficiency: It can be defined as the ratio of the power delivered to the secondary (suction) fluid to the power lost by the primary (inlet) fluid. In incompressible fluids, energy efficiency can be obtained as the product of the drag coefficient (C_d) and the pressure recovery ratio (PR) [37]. Since a compressible, ideal gas is considered here, this simplification is not valid and the equation (17) shall be used instead.

$$\eta = \frac{\dot{m}_s(e_d - e_s)}{\dot{m}_p(e_p - e_d)} \quad (17)$$

where:

- ed: Specific energy at the outlet or discharge port
- es: Specific energy at the secondary or suction port.
- ep: Specific energy at the primary or inlet port.

A central composite, faced-centered, and enhanced DOE was selected here, obtaining 17 treatments by each combination of two input parameters, P_i and P_j , as shown in Figure 9. As can be observed, five levels are deemed for each parameter (min, 1/4, 1/2, 3/4 and max) and the density of points is concentrated near the center (1/2, 1/2). In Table 5, the 89 computational experiments resulting from this DOE selection are shown.



Table 5. Results of Design of Experiments (DOE) for CFD simulations

Simulation number	Primary pressure, P_p (Pa)	Input parameters					Output performance parameters			
		λ	Rd	X	L1g	RA	Drag coefficient, C_d	Pressure ratio, PR	Energy Efficiency, η	
1.000	10000	0.01	5.00	4.00	1.00	10.00	0.17	0.02	0.22	
2.000	100000	0.01	5.00	4.00	3.00	10.00	0.02	0.02	0.01	
3.000	100000	0.01	5.00	7.00	1.00	10.00	0.02	0.02	0.01	
4.000	10000	0.01	5.00	7.00	3.00	10.00	0.23	0.02	0.27	
5.000	100000	0.01	7.50	4.00	1.00	10.00	0.02	0.02	0.04	
6.000	10000	0.01	7.50	4.00	3.00	10.00	0.29	0.02	0.63	
7.000	10000	0.01	7.50	7.00	1.00	10.00	0.31	0.02	0.64	
8.000	100000	0.01	7.50	7.00	3.00	10.00	0.09	0.02	0.08	
9.000	55000	0.16	6.25	5.50	2.00	10.00	0.23	0.02	0.22	
10.000	100000	0.30	5.00	4.00	1.00	10.00	0.15	0.02	0.11	
11.000	10000	0.30	5.00	4.00	3.00	10.00	0.32	0.02	0.38	
12.000	10000	0.30	5.00	7.00	1.00	10.00	0.33	0.02	0.41	
13.000	100000	0.30	5.00	7.00	3.00	10.00	0.17	0.03	0.13	
14.000	10000	0.30	7.50	4.00	1.00	10.00	0.35	0.02	0.60	
15.000	100000	0.30	7.50	4.00	3.00	10.00	0.19	0.10	0.16	
16.000	100000	0.30	7.50	7.00	1.00	10.00	0.20	0.05	0.17	
17.000	10000	0.30	7.50	7.00	3.00	10.00	0.34	0.03	0.59	
18.000	32500	0.08	5.63	4.75	1.50	15.00	0.24	0.02	0.27	
19.000	77500	0.08	5.63	4.75	2.50	15.00	0.15	0.02	0.13	
20.000	77500	0.08	5.63	6.25	1.50	15.00	0.16	0.02	0.14	
21.000	32500	0.08	5.63	6.25	2.50	15.00	0.25	0.02	0.26	
22.000	77500	0.08	6.88	4.75	1.50	15.00	0.19	0.02	0.18	
23.000	32500	0.08	6.88	4.75	2.50	15.00	0.27	0.03	0.35	
24.000	32500	0.08	6.88	6.25	1.50	15.00	0.27	0.02	0.37	
25.000	77500	0.08	6.88	6.25	2.50	15.00	0.19	0.03	0.18	
26.000	55000	0.16	6.25	5.50	2.00	15.00	0.24	0.03	0.23	
27.000	77500	0.23	5.63	4.75	1.50	15.00	0.21	0.04	0.17	
28.000	32500	0.23	5.63	4.75	2.50	15.00	0.28	0.04	0.28	
29.000	32500	0.23	5.63	6.25	1.50	15.00	0.28	0.03	0.30	
30.000	77500	0.23	5.63	6.25	2.50	15.00	0.21	0.05	0.15	
31.000	32500	0.23	6.88	4.75	1.50	15.00	0.29	0.04	0.37	
32.000	77500	0.23	6.88	4.75	2.50	15.00	0.21	0.08	0.18	
33.000	77500	0.23	6.88	6.25	1.50	15.00	0.22	0.04	0.20	
34.000	32500	0.23	6.88	6.25	2.50	15.00	0.28	0.06	0.34	
35.000	55000	0.01	6.25	5.50	2.00	20.00	0.13	0.02	0.12	
36.000	55000	0.08	6.25	5.50	2.00	20.00	0.23	0.03	0.22	
37.000	55000	0.16	5.00	5.50	2.00	20.00	0.22	0.02	0.19	
38.000	55000	0.16	5.63	5.50	2.00	20.00	0.24	0.03	0.21	
39.000	55000	0.16	6.25	4.00	2.00	20.00	0.24	0.04	0.23	
40.000	55000	0.16	6.25	4.75	2.00	20.00	0.24	0.04	0.23	
41.000	55000	0.16	6.25	5.50	1.00	20.00	0.25	0.03	0.25	
42.000	55000	0.16	6.25	5.50	1.50	20.00	0.25	0.04	0.24	
43.000	10000	0.16	6.25	5.50	2.00	20.00	0.34	0.03	0.51	
44.000	32500	0.16	6.25	5.50	2.00	20.00	0.28	0.04	0.31	
45.000	55000	0.16	6.25	5.50	2.00	20.00	0.24	0.04	0.23	
46.000	77500	0.16	6.25	5.50	2.00	20.00	0.21	0.04	0.18	
47.000	100000	0.16	6.25	5.50	2.00	20.00	0.19	0.03	0.15	
48.000	55000	0.16	6.25	5.50	2.50	20.00	0.25	0.03	0.24	
49.000	55000	0.16	6.25	5.50	3.00	20.00	0.24	0.04	0.23	
50.000	55000	0.16	6.25	6.25	2.00	20.00	0.24	0.04	0.23	
51.000	55000	0.16	6.25	7.00	2.00	20.00	0.24	0.04	0.23	
52.000	55000	0.16	6.88	5.50	2.00	20.00	0.25	0.04	0.25	
53.000	55000	0.16	7.50	5.50	2.00	20.00	0.25	0.10	0.26	
54.000	55000	0.23	6.25	5.50	2.00	20.00	0.25	0.06	0.26	
55.000	55000	0.30	6.25	5.50	2.00	20.00	0.25	0.16	0.23	
56.000	77500	0.08	5.63	4.75	1.50	25.00	0.18	0.02	0.15	
57.000	32500	0.08	5.63	4.75	2.50	25.00	0.27	0.02	0.28	
58.000	32500	0.08	5.63	6.25	1.50	25.00	0.27	0.02	0.30	
59.000	77500	0.08	5.63	6.25	2.50	25.00	0.19	0.03	0.16	
60.000	32500	0.08	6.88	4.75	1.50	25.00	0.29	0.03	0.38	
61.000	77500	0.08	6.88	4.75	2.50	25.00	0.20	0.03	0.18	
62.000	77500	0.08	6.88	6.25	1.50	25.00	0.20	0.03	0.19	
63.000	32500	0.08	6.88	6.25	2.50	25.00	0.28	0.03	0.35	
64.000	55000	0.16	6.25	5.50	2.00	25.00	0.25	0.04	0.24	
65.000	32500	0.23	5.63	4.75	1.50	25.00	0.29	0.07	0.30	
66.000	77500	0.23	5.63	4.75	2.50	25.00	0.22	0.09	0.17	
67.000	77500	0.23	5.63	6.25	1.50	25.00	0.22	0.10	0.17	
68.000	32500	0.23	5.63	6.25	2.50	25.00	0.28	0.11	0.28	
69.000	77500	0.23	6.88	4.75	1.50	25.00	0.22	0.30	0.19	
70.000	32500	0.23	6.88	4.75	2.50	25.00	0.28	0.43	0.32	
71.000	32500	0.23	6.88	6.25	1.50	25.00	0.29	0.14	0.35	
72.000	77500	0.23	6.88	6.25	2.50	25.00	0.22	0.20	0.18	
73.000	100000	0.01	5.00	4.00	1.00	30.00	0.02	0.02	0.01	
74.000	10000	0.01	5.00	4.00	3.00	30.00	0.25	0.02	0.30	
75.000	10000	0.01	5.00	7.00	1.00	30.00	0.23	0.02	0.29	
76.000	100000	0.01	5.00	7.00	3.00	30.00	0.02	0.02	0.01	
77.000	10000	0.01	7.50	4.00	1.00	30.00	0.30	0.02	0.61	
78.000	100000	0.01	7.50	4.00	3.00	30.00	0.11	0.02	0.09	
79.000	100000	0.01	7.50	7.00	1.00	30.00	0.08	0.02	0.07	
80.000	10000	0.01	7.50	7.00	3.00	30.00	0.32	0.02	0.62	
81.000	55000	0.16	6.25	5.50	2.00	30.00	0.25	0.06	0.23	
82.000	10000	0.30	5.00	4.00	1.00	30.00	0.34	0.02	0.42	
83.000	100000	0.30	5.00	4.00	3.00	30.00	0.19	0.32	0.13	
84.000	100000	0.30	5.00	7.00	1.00	30.00	0.19	0.07	0.15	
85.000	10000	0.30	5.00	7.00	3.00	30.00	0.33	0.12	0.37	
86.000	100000	0.30	7.50	4.00	1.00	30.00	0.21	0.34	0.17	
87.000	10000	0.30	7.50	4.00	3.00	30.00	0.34	0.06	0.45	
88.000	10000	0.30	7.50	7.00	1.00	30.00	0.35	0.03	0.54	
89.000	100000	0.30	7.50	7.00	3.00	30.00	0.19	0.19	0.14	



Table 6. Parameters of the Genetic Algorithm-based methods for the SO and MO optimization.

Parameters	Value
Number of initial samples	6000
Number of samples per iteration	1200
Maximum Allowable Pareto Percentage	70
Convergence Stability Percentage	2
Maximum Number of Iterations	20
Maximum number of Candidate Points	3

The Response Surface Optimization (RSO) Methodology is implemented here to seek the optimum points. The algorithm of genetic aggregation of ANSYS™ is used to obtain the response surface, whereas the Single-Objective and Multi-Objective Genetic Algorithms (SOGA and MOGA, respectively) are used for the optimization process. Four optimization cases are considered. In the first three types, the performance parameters (C_d , PR and η) are independently maximized in terms of the non-dimensional geometrical parameters previously defined (λ , R_d , X , L_{1g} and RA) for five inlet or primary gauge pressures, P_p (10 kPa, 25 kPa, 50 kPa, 75 kPa and 100 kPa) using SOGA. The fourth type of RSO optimization is a multi-objective optimization where performance parameters (C_d , PR and η) are simultaneously considered as objective functions using MOGA, assigning the same importance weight.

In optimization strategies based on genetic evolutionary algorithms, three basic aspects shall be considered: selection, crossover and mutation. Firstly, design points, coined as ‘chromosomes’, are randomly originated from the response surface and a selection operator is used for classifying and selecting the points leading to the better objective functions according to an objective-domination count. Then, once selected the initial ‘chromosomes’, a cross-over operator is applied to form new ‘chromosomes’, aimed to optimize the objective variables, and a mutation operator is used to continuously modified ‘genes’ of new ‘chromosomes’, avoiding stagnation at local optimum points [43, 44]. For continuous parameters, as the ones considered here, linear cross-over operators to generate new offspring are considered in ANSYS Fluent™:

$$Offspring1 = a \times Parent1 + (1 - a) \times Parent2 \tag{18}$$

$$Offspring2 = (1 - a) \times Parent1 + a \times Parent2 \tag{19}$$

where “a” is chosen to combine the best characteristics of each parent. Regarding the mutation, a polynomial mutation operator is implemented in ANSYS Fluent™ by defect:

$$C = P + (Upperbound - Lowerbound)\sigma \tag{20}$$

where C, P and σ represent the child, parent and small variation calculated from a polynomial, respectively. Once the new population is generated via cross-over and mutation, the response surface is used to compute the corresponding output parameters. This process of ‘natural selection’ is continuously repeated until convergence is reached or stopping criteria are met. The Maximum Allowable Pareto Percentage and the Convergence Stability Percentage are the convergence criteria considered here, whereas the Maximum Number of Iterations is the stopping criterion. Consequently, the controls of the Genetic Algorithm-based optimization methods (SOGA and MOGA) used in the present work are shown in Table 6. As can be observed, three candidate points are requested. For the SO optimizations, the candidate leading to the greater performance parameter is selected, whereas for the MO optimization, it is considered the one leading to the maximum energy efficiency, η .

4. Results and Discussion

4.1 Validation of CFD computational model

In order to evaluate the reliability of the numerical setup considered for the CFD simulations (Section 2), the jet pump configuration and boundary conditions deemed in Fen et al. [5] are taken into account, see Figure 10. In such work, an experimental setup was developed, where air was used as working fluid. In this sense, the primary, secondary and outlet pressures were regulated, with the former one varying from 300 kPa to 1000 kPa, and the other two fixed at 60 kPa and 80 kPa, respectively. Outlet and primary mass flow rate were directly measured, whereas the secondary mass flow rate was calculated as the difference between these ones. And, the local atmospheric pressure was measured as 96 kPa.

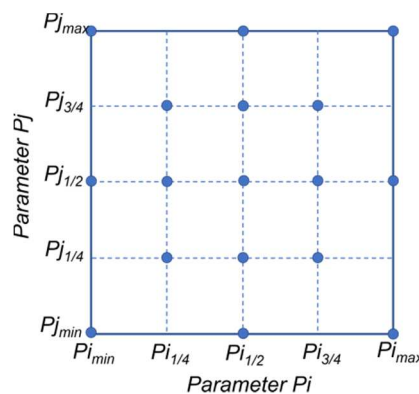


Fig. 9. Representation of Central Composite, faced-centered, enhanced DOE.



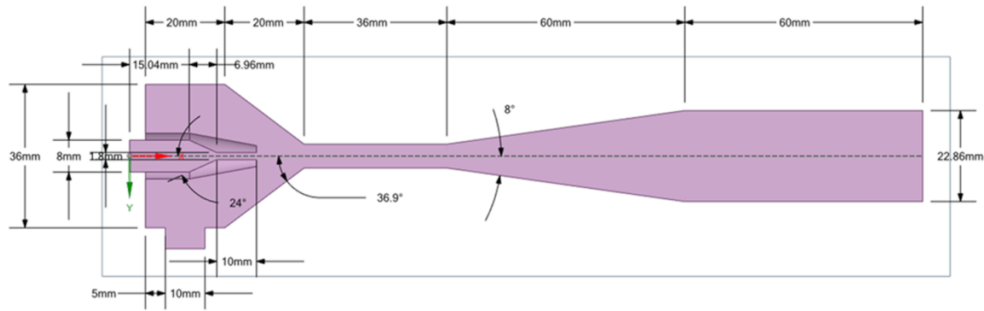


Fig. 10. Geometrical configuration and dimensions of jet pump for validation.

Several similitudes and differences between the numerical configuration of Fen et al. [5] and the one used in the present work can be identified. For instance, in Fen et al [5] the complete three-dimensional domain was simulated, ideal gas was assumed and the Shear Stress Transport (SST) $k-\omega$ turbulence model was used; additionally, it was employed a pressure-based solver with the following characteristics: SIMPLEC algorithm for the solution of the pressure-velocity field, least-square cell-based scheme for calculation of gradient terms, second-order scheme for pressure interpolation, second-order upwind for density, momentum, turbulent kinetic energy, turbulent dissipation rate and energy. Otherwise, in the present work, a symmetry condition is implemented to simulate the half domain, ideal gas assumption is valid as well, $k-\epsilon$ turbulence model with Enhanced Wall Treatment is used, and the principal configuration characteristics of the pressure-based solver are similar to the ones used in Fen et al. [5], with exception of the solution scheme of the pressure-velocity field, which is chosen here as coupled, and the introduction of high order relaxation terms. Moreover, in Fen et al. [5], a hexahedral mesh is used and mesh refinement near the nozzle wall is not implemented. In the present work, mesh is formed by Tet4 and Wed6 elements, with inflation elements near the nozzle wall to better reproduce the effects of the boundary layer.

In this point, it is important to highlight that one of the main differences between the work of Fen et al [5] and the present work is the turbulence model used. Firstly, it is important to mention that both the $k-\epsilon$ and $k-\omega$ STT models are two-equations RANS models based on Boussinesq hypothesis that have been widely used in fluid flow simulations of jet pumps, as can be observed in Table 7, where turbulence models employed in some works are presented. Accordingly, the $k-\omega$ STT model can produce reliable solutions for the boundary layer and freestream flow, since it resembles the standard $k-\omega$ model for some points inside the viscous and logarithmic sublayers, and the $k-\epsilon$ model for points in the freestream region. This model is more robust than $k-\epsilon$, but it is computationally more expensive, since it involves more calibration parameters and it is more sensitive to such calibration. Nevertheless, the $k-\epsilon$ standard model is particularly recommended for freestream flow with high turbulent Reynolds number, since it provides a good trade-off between robustness, time-consumption and accuracy; additionally, this model demands less number of calibration parameters, and the standard values of these parameters (see Table 3) have shown to be suitable in many industrial applications. Thus, to obtain a reasonable accuracy of the fluid flow solution in the boundary layer with the $k-\epsilon$ standard model, the addition of inflation elements to the mesh aiming to obtain satisfactory values of y^+ in the viscous and logarithmic sublayers, and the selection of Enhanced Wall Treatment functions, are appropriated strategies.

In Table 8, the present results and those experimentally and numerically obtained by Fen et al [5] are shown. The L^2 relative error norm can be used to compare these results among them, computed as follows:

$$L^2 = \sqrt{\frac{\sum_{j=1}^m [(\dot{m}_{pj}^{REF} + \dot{m}_{sj}^{REF}) - (\dot{m}_{pj}^{(PRESENT)} + \dot{m}_{sj}^{(PRESENT)})]^2}{\sum_{j=1}^m (\dot{m}_{pj}^{REF} + \dot{m}_{sj}^{REF})^2}} \tag{21}$$

Table 7. Turbulence models used in several CFD simulations of jet pumps.

Research work	Turbulence models
Present work	$k-\epsilon$ standard
Orozco et al. [18]	$k-\epsilon$ standard
Fen et al. [5]	$k-\omega$ SST
Yapici and Aldas [29]	* $k-\epsilon$ standard * $k-\epsilon$ realizable * RSM * $k-\omega$ SST
Aldas and Rapici [45]	$k-\omega$ SST
Shah, Chughtai and Inayat [27]	$k-\epsilon$ realizable
Song et al. [28]	RNG $k-\epsilon$ model
Dong, Wang and Tu [46]	* $k-\epsilon$ standard * $k-\epsilon$ realizable * RSM * $k-\omega$ SST
Zheng, Li and Qin [30]	$k-\epsilon$ standard
Deng et al. [31]	* $k-\epsilon$ standard * $k-\epsilon$ realizable * $k-\epsilon$ RNG
Varga et al. [37]	$k-\epsilon$ realizable
Thongtip and Aphornratana [9]	$k-\epsilon$ realizable
Masud and Inram [47]	$k-\epsilon$ standard



Table 8. Comparison between present CFD results and results obtained by Fen et. al [5]

Primary or inlet pressure, P_p (kPa)	Numerical model of Fen et. al [5]		Experimental results of Fen et. al [5]		Present numerical model	
	Primary Mass flow rate (g/s)	Secondary mass flow rate (g/s)	Primary Mass flow rate (g/s)	Secondary mass flow rate (g/s)	Primary Mass flow rate (g/s)	Secondary mass flow rate (g/s)
1000.00	6.04	7.29	6.41	7.15	6.15	7.07
900.00	5.49	7.15	5.84	7.01	5.65	6.86
800.00	4.97	7.05	5.30	6.88	5.08	6.64
700.00	4.39	6.60	4.62	6.43	4.51	6.36
600.00	3.84	6.08	4.13	5.90	3.94	5.78
500.00	3.29	5.41	3.48	5.25	3.37	4.94
400.00	2.76	4.22	2.92	3.99	2.80	3.83
350.00	2.48	3.37	2.64	3.21	2.52	3.07
300.00	2.29	2.24	2.30	2.12	2.23	2.02

Table 9. Classification of correlation intensity according to [48].

Qualitative description	Value
Very weak	0.00-0.19
Weak	0.20-0.39
Moderate	0.40-0.59
Strong	0.60-0.79
Very strong	0.80-1.00

where \dot{m}_{pj}^{REF} and \dot{m}_{sj}^{REF} represent the primary and secondary mass flow rate, for the inlet pressure case “j”, retrieved from the reference work [5] (both numerically and experimentally), whereas $\dot{m}_{pj}^{PRESENT}$ and $\dot{m}_{sj}^{PRESENT}$ are the corresponding mass flow rates obtained in the present work. Accordingly, when comparing present solutions with numerical solutions of Fen et al [5], relative error is $L^2=4.80E-2$, whereas an error of $L^2=3.31E-2$ is achieved regarding experimental results. This shows that the present numerical configuration of the CFD simulations is reliable to conduct this kind of analysis.

4.2 DOE results and correlation analysis

Simulation experiments and corresponding results of Design of Experiments (DOE) are represented in Table 5, where one processing input parameter (Primary or inlet pressure, P_p), five non-dimensional geometrical parameters (λ , R_d , X , L_{1g} and RA) and the three performance output parameters (C_d , PR and η) can be distinguished. In the present section, a correlation analysis between the input and output parameters is carried out. As an initial screening, the Spearman Rank-order correlation matrix, represented in Figure 11, is analyzed. According to these results and the classification of correlation intensity given in Table 9, correlation between drag coefficient (C_d) and primary pressure (P_p) is very strongly negative (correlation coefficient of -0.84), as well as the correlation between energy efficiency (η) and primary pressure (correlation coefficient of -0.92). Besides, a negative correlation between the pressure recovery ratio (PR) and parameter X can be identified, but this is very weak (-0.13), which means that the relationship between these variables can be dependent on the level of the other parameters. A very weak positive correlation can be noticed between drag coefficient, C_d , and parameters R_d (0.12) and RA (0.16), between the pressure recovery ratio, PR , and parameters P_p (0.16) and L_{1g} (0.17), and between energy efficiency, η , and parameter λ (0.15). On the contrary, correlations $PR-R_d$ (0.22), $PR-RA$ (0.39), and $\eta-R_d$ (0.23) can be deemed weak positive, whereas correlations $C_d-\lambda$ (0.42) and $PR-\lambda$ (0.72) can be considered moderate and strong, respectively.

Now, a local sensitivity analysis is carried out. This analysis allows depicting the independent influence of one input variable on the performance parameters when the other input variables are kept constant at determined level. In Figures 12a-c, the local sensitivity bar plots corresponding to the lower ($\lambda=0.01$, $R_d=5$, $X=4$, $L_{1g}=1$, $RA=10$), intermediate ($\lambda=0.15$, $R_d=6.25$, $X=5.5$, $L_{1g}=2$, $RA=20$) and upper levels ($\lambda=0.3$, $R_d=7.5$, $X=7$, $L_{1g}=3$, $RA=30$) of the non-dimensional input parameters are shown. The jet pump geometries equivalent to these three levels are shown in Figure 13. By doing so, the following results are common for these three levels (see Figure 12a-c):

- Drag coefficient, C_d , and energy efficiency, η , are inversely proportional to the inlet pressure, P_p , and directly proportional to parameter λ . This means that these performance parameters (C_d and η) increase when diameter of nozzle outlet increases regarding diameter of nozzle throat. Additionally, this also allows inferring that a convergent-divergent nozzle can be better than an only-convergent one (see Figure 1) for this application of vacuum distillation.
- Drag coefficient, C_d , and energy efficiency, η , are directly proportional to parameter R_d , but this proportionality decreases with the input variables levels; in such a way, it is very small at the upper level (Figure 12c). From the definition of R_d in equation (9), this means that the longer the divergent section of the diffuser regarding the diameter of straight part, the superior the values of C_d and η .

On the other hand, the influence of X , L_{1g} and RA on the drag coefficient (C_d) seems to be similar to the influence on the energy efficiency (η), being dependent on the level of the input variables. In general, C_d and η are directly proportional to these three input variables (X , L_{1g} and RA) for the lower level (Figure 12a). Besides, for the intermediate level (Figure 12b), the influence of X and L_{1g} on C_d and η are practically negligible, whereas RA shows low direct proportionality with C_d . For the upper level (Figure 12c), influence of X , L_{1g} and RA on C_d and η is not very significant.

Additionally, for the pressure ratio, PR , numerical results show a non-significant influence of the input variables on this performance parameter for the lower level (Figure 12a). And, for the intermediate level (Figure 12b), an important direct proportionality is noticeable with λ , R_d and RA , whereas for the upper level (Figure 12c), all input variables have a notorious influence on the pressure ratio, PR , with X decreasing this performance parameter, and the remaining input variables, increasing it.

In this point, it is very important to highlight that the aforementioned observations are valid as long as one input parameter changes while the others remain constant.



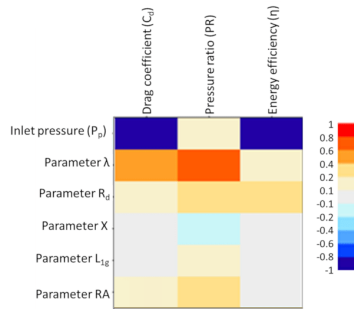


Fig. 11. Spearman Rank-order correlation matrix for DOE of CFD simulations.

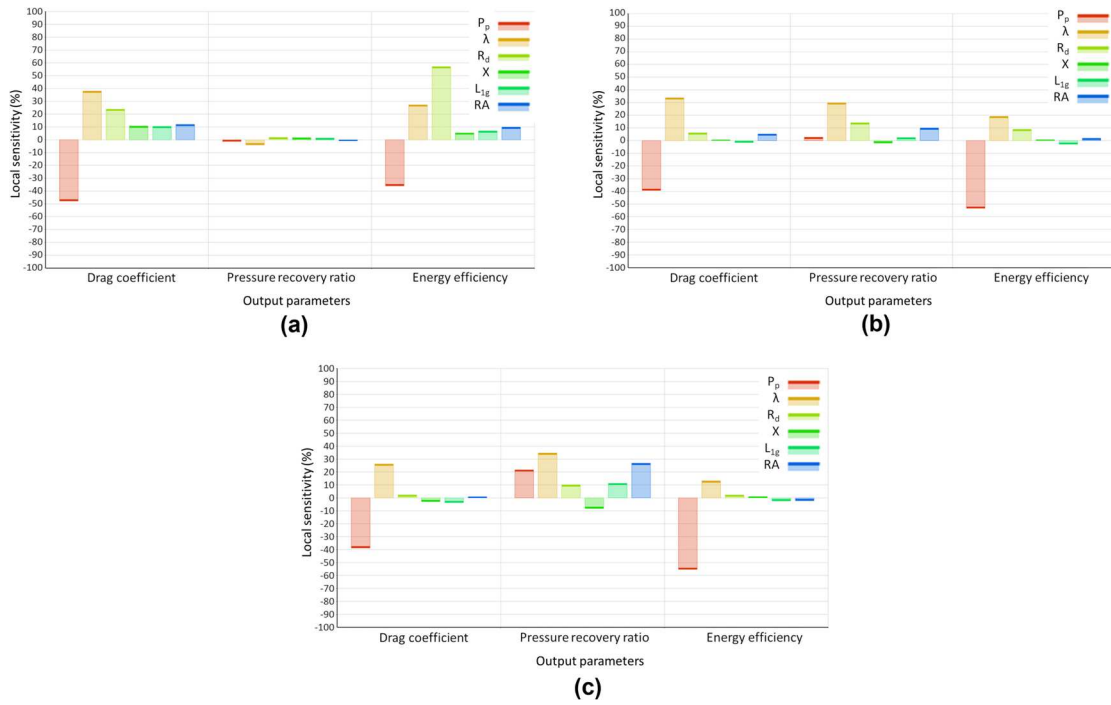


Fig. 12. Local sensitivity analysis. a) Lower level of input variables, b) Intermediate level of input variables, c) Upper level of input variables.

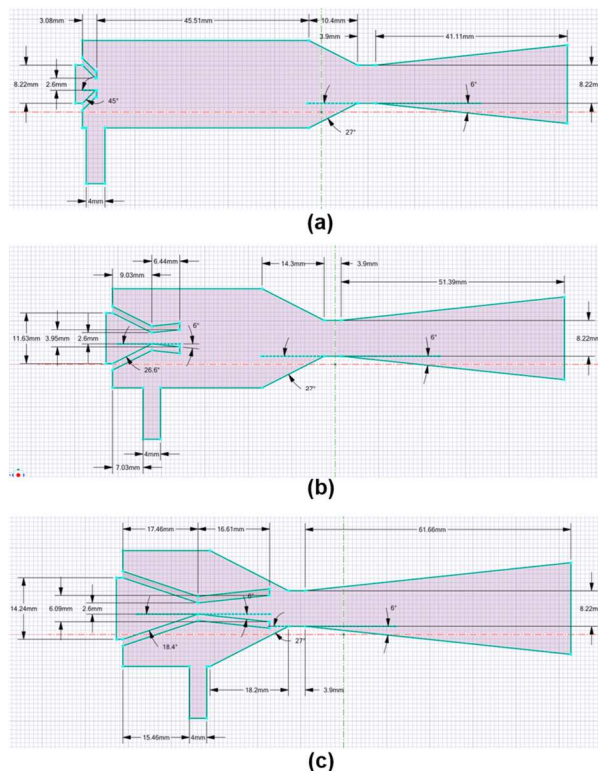


Fig. 13. Geometries of the jet pump corresponding to several levels of the geometrical non-dimensional parameters. a) Lower level, b) Intermediate level, c) Superior level.



4.3 Results of response surface optimization

In the present section, results of the single-objective (SO) and multi-objective (MO) optimizations are presented and discussed. In Sections 4.3.1 to 4.3.4, the influence of the inlet pressure, P_p , on the optimized non-dimensional parameters (λ , R_d , X , L_{1g} and RA) and the optimized performance parameters (C_d , PR and η) is studied. Also, in the section 4.3.5, the behavior of the performance parameters (C_d , PR and η) with the area ratio (RA), considering the remaining input parameters as slice parameters, starting from the jet pump geometry corresponding to the MO optimization, is analyzed. Finally, in section 4.3.6, the behavior of the Mach number in the fluid domain for the jet pump geometries that maximize the energy efficiency, η , considering several inlet pressures, P_p , is analyzed.

4.3.1 Single-objective optimization of drag coefficient

In Figure 14, the values of the geometrical non-dimensional parameters that maximize the drag coefficient, C_d , for several inlet pressures, P_p are shown. This way, in optimizing the drag coefficient, C_d , for the entire pressure range analyzed here (10 to 100 kPa), the optimum values of parameters R_d and X are not significantly affected by the inlet pressure, P_p , since they remain in a narrow range of variability (between 0.36 and 0.38). However, the optimum values of λ , L_{1g} and RA show a non-monotonic variation with the inlet pressure, P_p , with RA as the most changeable parameter. Regarding this, it is important to realize that maximum and minimum values of the optimized parameter RA are reached in intermediate pressures, P_p , with the maximum value obtained for 25 kPa and the minimum for 75 kPa. Also, from the definition of the non-dimensional parameters in Section 3, this means that the optimum nozzle shape is highly dependent on the working pressure of the jet pump, conversely to the other optimized dimensions of the jet pump. Accordingly, the optimization of the following nozzle characteristics is very influenced by the inlet pressure, P_p : outlet diameter and length of the divergent part, conicity angle of convergent part, and ratio between the areas of the inlet (A_1) and throat (A_g), RA . As can be observed in Figure 14, the optimum drag coefficient, C_d , decreases with the inlet pressure, P_p , confirming the results of correlation and local sensitivity analyses formerly presented. It is worth-noticeable as well that for a same area ratio, RA , different optimum values of C_d can be obtained depending on the inlet pressure (see for instance optimum values of RA and the corresponding values of C_d for the two extreme inlet pressures, 10 kPa and 100 kPa).

4.3.2 Single-objective optimization of pressure recovery ratio

The values of the geometrical non-dimensional parameters that maximize the pressure recovery ratio, PR , are shown in Figure 15. As for the drag coefficient (Figure 14), the optimum parameter that changes evidently with the inlet pressure, P_p , is the area ratio RA (between 25 and 29), although a monotonic incremental variation is observed in this case. This variation implies that the higher the inlet pressure, the larger shall be the ratio between the areas of the inlet (A_1) and throat (A_g) of nozzle to maximize the pressure recovery ratio, PR , of the jet pump. Furthermore, the change of the remaining optimum parameters with the inlet pressure, P_p , is not significant. As can be observed in Figure 15, the optimum pressure recovery ratio, PR , increases with the inlet pressure, P_p . In general, the optimized values of PR are in a narrower range than those ones of C_d (see Figure 14) and this behavior can be explained by the small variability of most of the optimum geometrical parameters with P_p in the present case.

4.3.3 Single-objective optimization of energy efficiency

In Figure 16, the values of the geometrical parameters that maximize the energy efficiency, η , as a function of the inlet pressure, P_p are shown. In a similar fashion, as for the drag coefficient, C_d (Figure 14), optimum values of parameters R_d and X show small variability with the inlet pressure, P_p . In fact, this observation is extensible to the parameter L_{1g} . On the other hand, a non-monotonic change of optimum parameters λ and RA with the inlet pressure, P_p , can be noticed. This means that the inlet pressure, P_p , has a relevant influence on the efficiency optimization of the outlet diameter and length of divergent part of nozzle, and area ratio RA . As can be observed in Figure 16, the optimum energy efficiency, η , shows a significant reduction with the inlet pressure, P_p .

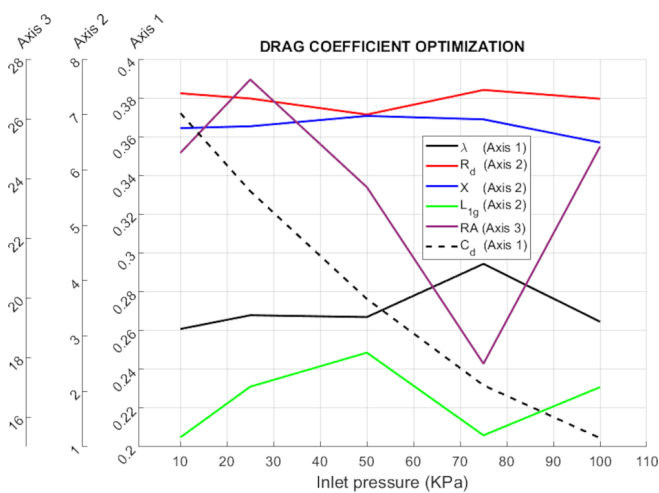


Fig. 14. Optimum non-dimensional parameters that maximize the drag coefficient for several inlet pressures.

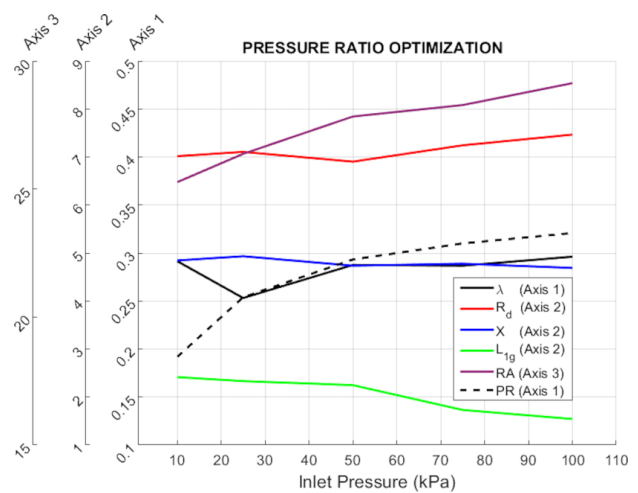


Fig. 15. Optimized input parameters that maximize the pressure recovery ratio for several inlet pressures.



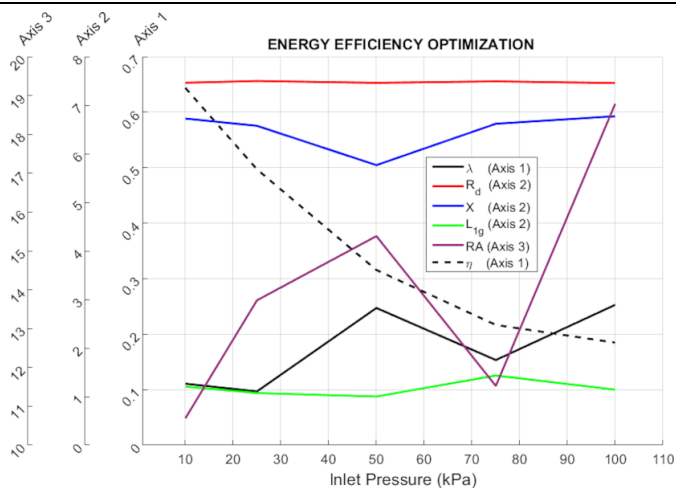


Fig. 16. Optimized input parameters that maximize the energy efficiency for several inlet pressures.

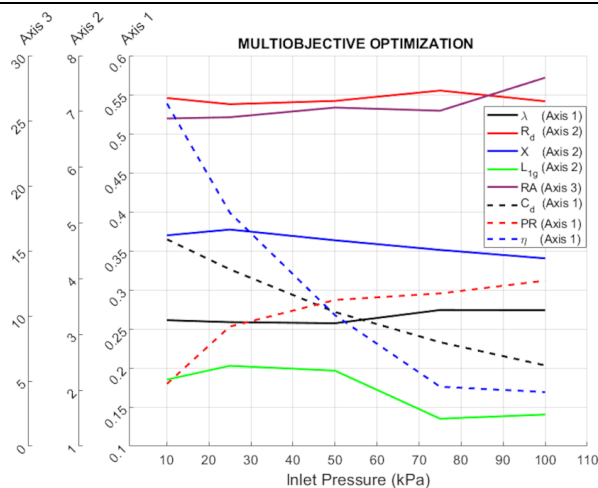


Fig. 17. Optimized input parameters for the multi-objective optimization for several inlet pressures.

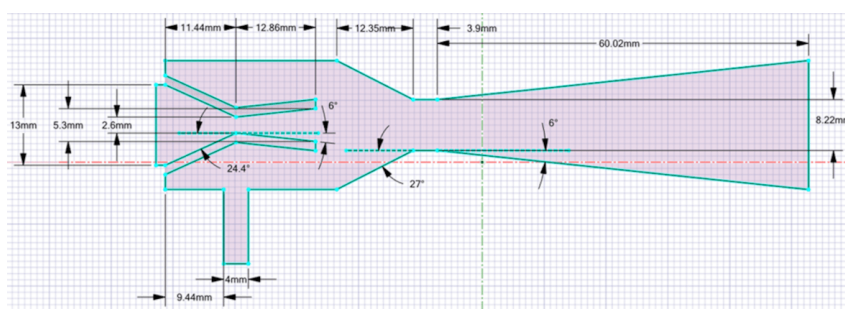


Fig. 18. Optimum jet pump geometry corresponding to average non-dimensional parameters of multi-objective optimization.

4.3.4 Multi-objective optimization of performance parameters

The values of the geometrical non-dimensional parameters corresponding to the multi-objective optimization, for several inlet pressures, P_p , are shown in Figure 17. In this point, it is important to remember that the same importance weight was assigned to each performance parameter (C_d , PR and η), and that the energy efficiency, η , cannot be directly computed from the other two parameters (C_d and PR), since fluid flow is compressible. As can be observed in Figure 17, no significant changes of any of the optimized geometrical parameters are observed, which means that inlet pressure, P_p , does not have a significant influence on the optimum geometry of the jet pump in this particular case. However, it is observed that the behavior of the performance parameters (C_d , PR and η) with the inlet pressure, P_p , is the same as the one appreciated in the abovementioned cases, namely, optimum values of C_d and η decrease with P_p , whereas optimum value of PR increases. Also, this means that despite the optimized geometry is almost the same for all inlet pressures, P_p , considered here, the values of performance parameters achieved for this geometry are sensitive to the working pressure, P_p . Thus, the jet pump geometry corresponding to the average values of the optimized non-dimensional parameters of Figure 17 is shown in Figure 18.

4.3.5 Parametric study on the jet pump performance for the multi-objective optimization

As it was aforementioned in Section 4.3.4, the optimum values of the non-dimensional geometrical parameters (λ , R_d , X, L_{1g} and RA) for the MO optimization are basically independent on the working pressure, P_p . The jet pump geometry corresponding to the average values of these parameters is represented in Figure 18. In the present section, the area ratio (RA) of this geometry is modified, and an additional non-dimensional parameter is taking as slice parameter, keeping constant the remaining ones. In this way, the purpose of the present section is to study the change of the performance parameters (C_d , PR and η) with RA for several levels of the other parameters. The 2D-slice plots represented in Figure 19 are obtained.

The behavior of the drag coefficient, C_d , with RA for several levels of λ is shown in Figure 19a. As can be observed, C_d increases with RA for most of the values of λ (except for $\lambda=0.3$), and the behavior of C_d with λ , for a constant value of RA, is not uniform, with the level corresponding to $\lambda=0.267$ as the one where maximum values of C_d are reached. Maximum value of C_d is gotten for this level of λ and the maximum area ratio, RA=30. Therefore, these results show that the increment of the area ratio, RA, usually leads to the increase of C_d , with some exceptions depending on the outlet diameter and the length of the divergent part of the nozzle.

In the case of pressure ratio (PR), Figure 19b, it can be observed that PR increases with the area ratio, RA, up to a maximum value of RA = 26 for most of the values of λ . As for the drag coefficient (Figure 19a), for a constant value of RA, the behavior of PR with λ is not uniform, with the level corresponding to $\lambda=0.267$ as such where the maximum PR is reached. Then, in the case of energy efficiency (η), Figure 19c, this performance parameter (η) shows a decreasing behavior with RA for all values of λ , whereas the behavior of η with λ for a constant value of RA is not uniform as well. As a result, the maximum jet pump efficiency is obtained for $\lambda = 0.1067$ and RA=10.

The behavior of the performance parameters (C_d , PR and η) with RA considering slices of parameter R_d (Figures 19d-f) is similar to the one observed in previous cases (Figures 19a-c), but an important difference can be identified: the increase of C_d with RA arises for all values of R_d . Additionally, it is worth-noting that the change of C_d and η with R_d , for a constant value of RA, is monotonous increasing, with greater changes as R_d is smaller. Maximum values of the performance parameters are obtained in the following levels: $R_d=7.5$ and RA=30 for C_d , $R_d=6.94$ and RA=26 for PR, and $R_d=7.5$ and RA=10 for η .



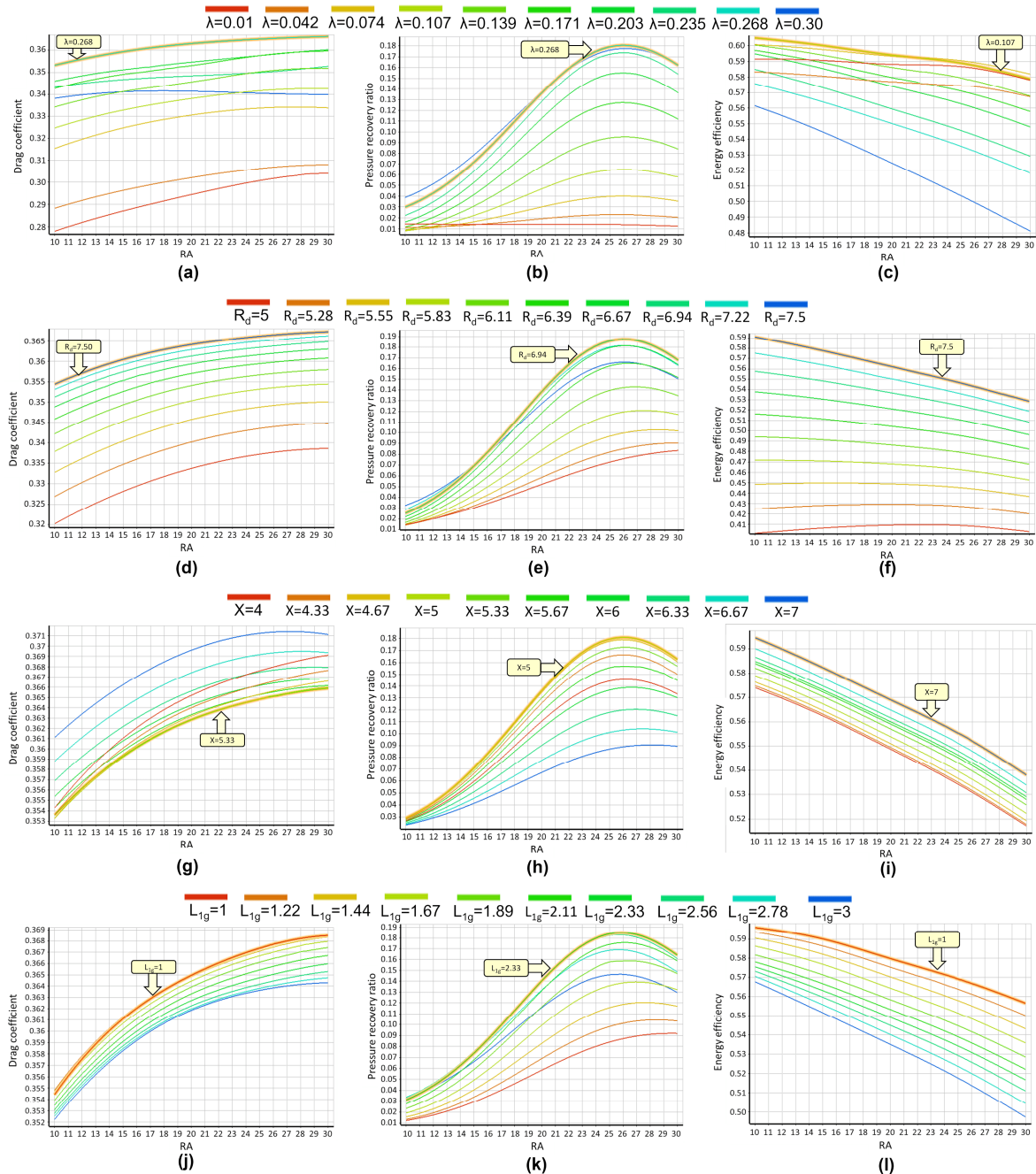


Fig. 19. Change of the performance parameters (C_d , PR and η) with RA, considering several levels of the remaining non-dimensional parameters.

Considering X as the slice parameter, Figures 19h and 19i show that performance parameters PR and η change with RA in a similar fashion as the cases of Figure 19e and 19f, respectively, with larger decreasing slopes for the efficiency, η , as shown in Figure 19i. For the drag coefficient, C_d (Figure 19g), contrarily to results of Figure 19d, the behavior of this performance parameter with RA is not monotonous increasing for all values of the slice parameter (X in this case). For a constant value of RA, only the efficiency, η , increases with X (Figure 19i). Maximum values of the performance parameters are obtained in the following levels: $X=7$ and $RA=27$ for C_d ; $X=5$ and $RA=26$ for PR, and $X=7.0$ and $RA=10$ for η .

For the slice parameter L_{1g} , Figures 19j-l, the variation of the performance parameters (C_d , PR and η) with RA is similar to the one obtained for the slice parameter R_d (Figures 19d-f). For a constant value of RA, change of C_d and η with L_{1g} are predominantly decreasing, whereas change of PR is non-monotonic. Maximum values of the performance parameters are obtained in the following levels: $L_{1g}=1$ and $RA=30$ for C_d , $X L_{1g}=2.33$ and $RA=26$ for PR, and $L_{1g}=1$ and $RA=10$ for η .

Finally, it is important to realize that the curves of PR vs. RA (Figures 19b, 19e, 19h and 19k) show a notorious local maximum for most of the slice parameters, which is not valid for curves of C_d vs. RA and η vs. RA. These differences in the behavior of the performance parameters are not expected for incompressible fluids, where η is directly computed from the other two parameters (C_d and PR); however, for incompressible fluids, this can be acceptable since fluid density along the domain is varying with pressure and temperature. Accordingly, while the pressure recovery ratio, PR, is only dependent on an intensive property (pressure), the other two performance parameters (C_d and η) also depend on the mass flow rates at the primary and secondary ports. Considering that P_p and P_s are prescribed values in the present work, and from definition of PR in equation (16), it can be inferred that maximum PR is reached when the discharge pressure, P_d , is maximum as well. However, maximization of P_d does not necessarily imply the maximization of the other two performance parameters, C_d and η , because they are not exclusively dependent on this pressure, but also on primary and secondary mass flow rates that, in turns, are highly influenced by the fluid density.



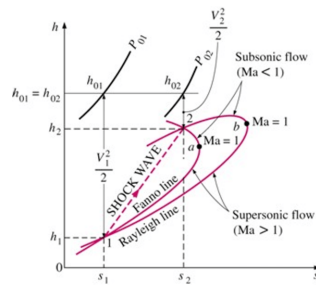


Fig. 20. h-s diagram for a flow that undergoes a normal shock [49].

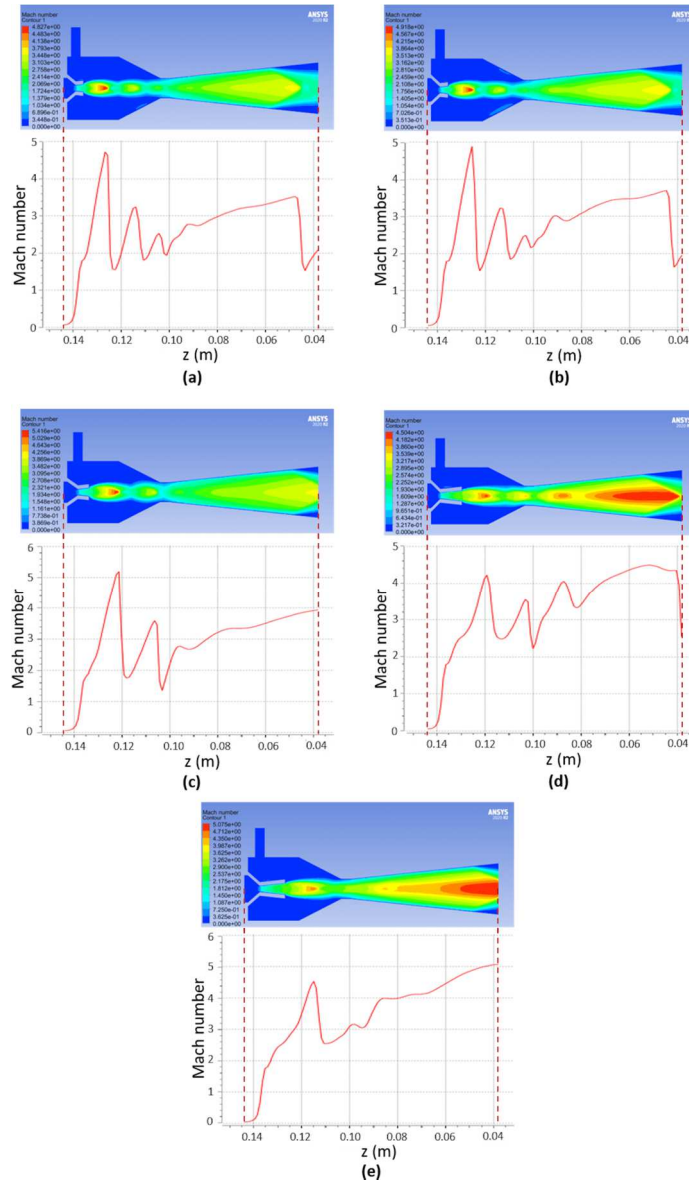


Fig. 21. Behavior of the Mach number in the fluid domain, a) $P_p=10$ kPa, b) $P_p=25$ kPa, c) $P_p=50$ kPa, d) $P_p=75$ kPa, e) $P_p=100$ kPa.

4.3.6 Mach number behavior for optimum geometries

In ideal conditions, fluid in the jet pump is isentropic, with subsonic characteristics up to the nozzle throat, and sonic and supersonic between the nozzle throat and the diffuser throat, reaching the highest Mach number at the nozzle outlet, with a gradual decrease until the straight part of the diffuser (See Figure 2a). The Enthalpy (h) vs. Entropy (s) curve corresponding to the ideal jet pump operation is shown in Figure 20. It is observed that the points of maximum entropy of Fanno and Rayleigh line (points a and b, respectively) correspond to a Mach number of $Ma=1$; points above this threshold are in the subsonic regime, while the points below, in the supersonic one. It is also observed that the Fanno and Rayleigh lines intersect at two points (points 1 and 2), which represent the two states at which the three conservation equations are satisfied. In State 1, primary and secondary fluid are separated, whereas in State 2, fluid collision takes place [49]. In the same sense, in ideal conditions of jet pumps for vacuum applications, the maximum Mach number is reached in point 2. If the flow at the nozzle outlet is supersonic and it is before a normal shock wave, a fast decreasing of the Mach number is expected and flow tends to subsonic regime. This situation is favorable



for the operation of the jet pump for vacuum generation, since it benefits the drag of the secondary fluid. On the other hand, if the flow at the nozzle outlet is supersonic and it is before an oblique shock wave, Mach number reduction is not so pronounced and this can considerably increase up to the diffuser outlet, even exceeding the value reached at the nozzle outlet. In fact, this situation is advantageous for the use of jet pumps in space shuttles, in supersonic aircraft or in propulsion rockets, but it is not totally convenient for vacuum generation.

The behavior of the Mach number in the fluid domain for the jet pump geometries that maximize the energy efficiency, considering several inlet pressures (10 kPa, 25 kPa, 50 kPa, 75 kPa and 100 kPa), can be observed in Figure 21. Bearing in mind the previous explanation, for the primary pressures of 10kPa, 25kPa and 50kPa, see Figures 21a-c, the jet pump operates in normal conditions for vacuum generation, since the maximum Mach number is obtained at the nozzle outlet. From these three cases, maximum Mach number is obtained for $P_p=50$ kPa ($Ma>5$). On the other hand, for $P_p=75$ kPa and $P_p=100$ kPa, see Figures 21d-e, the behavior of the jet pump is more applicable for propulsion, since the maximum Mach number is obtained near the diffuser outlet, but this type of behavior is not of interest in the present work.

5. Conclusions

In the present work, single-objective (SO) and multi-objective (MO) optimizations of a jet pump used for vacuum distillation of ethanol were accomplished considering five non-dimensional input variables (λ , R_d , X , L_{1g} and RA) and three performance output parameters (C_d , PR and η), for several working pressures, P_p . Besides, the CFD simulation setup was validated with numerical and experimental results, obtaining satisfactory results. Main conclusions about the influence of non-dimensional parameters and inlet pressure on the jet pump performance can be summarized as follows:

- Parameter λ : the optimum value of this parameter is dependent on the inlet pressure, P_p , for the SO optimization of C_d and η . Both C_d , PR and η increases with λ up to a certain threshold, from which they start decreasing. This means that convergent-divergent nozzles can be more suitable for this vacuum application than the only-convergent ones.
- Parameter R_d : for both SO and MO optimizations, the optimum value of R_d is not substantially influenced by the inlet pressure, P_p . There is a positive correlation between R_d and parameters C_d and η , but the intensity of this correlation is lower as other non-dimensional parameters are greater.
- Parameter X : inlet pressure, P_p , does not have an important effect on the optimum value of X . This parameter X affects the three performance parameters (C_d , PR and η), but this influence highly depends on the level of the remaining parameters.
- Parameter L_{1g} : the optimum value of this parameter is dependent on the inlet pressure, P_p , for the SO optimization of C_d . Starting from the jet pump geometry obtained in the MO optimization, the decrease of L_{1g} , keeping the remaining parameters constant, and leading to the increase of C_d and η .
- Parameter RA : for the three kinds of SO optimizations considered here (C_d , PR and η), the optimum value of RA is highly dependent on the inlet pressure, P_p . All results allow to infer that RA is the most influential parameter on the jet pump performance. Starting from the jet pump geometry corresponding to MO optimization, increasing RA , while maintaining the other parameters in a constant way and leading to greater values of C_d and lower values of η .
- Inlet pressure: for a determined jet pump geometry, both C_d and η tend to decrease with P_p . A well-defined relationship between PR and P_p was not obtained. On the other hand, the larger P_p , the lower the optimum values of C_d and η , and the greater the optimum value of PR .
- As a general statement, it can be emphasized that in jet pumps for vacuum distillation applications, the parameter having the greatest influence on their optimal operation is RA , namely, the ratio between nozzle inlet and nozzle throat areas, but this influence depends on the values of the other parameters. Therefore, it is recommended for jet pump designers to meticulously study the change of the jet pump performance in terms of this parameter RA by means of prototype testing and/or computational simulations, at several values of the others four non-dimensional parameters considered here (λ , R_d , X and L_{1g}).

Author Contributions

W.O. Murillo developed the computational modeling, examined the theory validation. I.D. Patiño Arcila planned the optimization scheme and analyzed the computational results. J.A. Palacio-Fernández compared the results of the numerical simulations with other experimental and numerical results. The manuscript was written with the contribution of all authors. All authors discussed the results, reviewed and approved the final version of the manuscript.

Acknowledgement

The authors are gratefully acknowledged to the Institución Universitaria Pascual Bravo, Facultad de Ingeniería, Grupo de Investigación e Innovación Ambiental (GIAM) and the Dirección de Tecnología e Innovación for their collaboration in the realization of this project.

Conflict of Interest

We declare that we have no significant competing interests including financial or non-financial, professional, or personal interests interfering with the full and objective presentation of the work described in this manuscript.

Funding

The authors received no financial support for the research, authorship, and publication of this article.

Data Availability Statements

The datasets generated and/or analyzed during the current study are available from the corresponding author on reasonable request.



Nomenclature

A_g	Nozzle throat area [m ²]	L_{mix}	Length of mixing chamber [m]
A_p	Nozzle entry area [m ²]	\dot{m}_p	Primary mass flow rate [kg/s]
C_d	Drag coefficient	\dot{m}_s	Secondary mass flow rate [kg/s]
D_o	Diameter of Diffuser discharge [m]	P_d	Discharge Pressure [kPa]
D_1	Diameter of nozzle inlet [m]	P_p	Inlet pressure [kPa]
D_2	Diameter of nozzle outlet [m]	PR	Pressure recovery ratio
D_g	Diameter of nozzle throat [m]	P_s	Suction or secondary pressure [kPa]
D_p	Diameter of suction chamber [m]	Ma	Mach number
D_t	Diameter of straight part of diffuser [m]	RA	Ratio between the areas of the inlet and throat of the nozzle
e_d	Specific energy at the outlet or discharge port	R_d	Ratio between the length of divergent part of the diffuser and diameter of the straight part of the diffuser
e_p	Specific energy at the primary or inlet port	X	Ratio between the length of the mixing chamber and the diameter of the nozzle throat
e_s	Specific energy at the secondary or suction port	α	Convergence angle of the diffuser [degrees]
L	Straight part of the diffuser [m]	β	Nozzle discharge angle [degrees]
L_{1g}	Ratio between the length of convergent part of the nozzle and half difference between diameters of inlet and throat nozzle	θ	Angle of diffuser discharge [degrees]
L_{conv}	Length of convergent part of the nozzle	λ	Range the diameter of the nozzle outlet between such of the nozzle throat and the one of nozzle inlet
L_{div}	Length of divergent part of diffuser [m]	η	Energy efficiency

References


- [1] Dong, S., Zeng, C., Ariaratnam, S. T., Ma, B., Yan, X., Li, Z., Li, X. Experimental and performance analysis of reverse circulation reaming in horizontal directional drilling, *Tunneling and Underground Space Technology*, 95, 2019, 103128.
- [2] Brendelberger, S., Von Storch, H., Bulfin, B., Sattler, C. Vacuum pumping options for application in solar thermochemical redox cycles – Assessment of mechanical-, jet- and thermochemical pumping systems, *Sol. Energy*, 141, 2017, 91–102.
- [3] Xu, M., Ji, B., Zou, J., Long, X. Experimental investigation on the transport of different fish species in a jet fish pump, *Aquac. Eng.*, 79, 2017, 42–48.
- [4] Pellegrini, M., Preda, G., Saccani, C. Application of an innovative jet pump system for the sediment management in a port channel: Techno-economic assessment based on experimental measurements, *J. Mar. Sci. Eng.*, 8, 2020, 686.
- [5] Feng, J., Han, J., Hou, T., Peng, X. Performance analysis and parametric studies on the primary nozzle of ejectors in proton exchange membrane fuel cell systems, *Energy Sources, Part A Recover. Util. Environ. Eff.*, 2020, 1–20, doi: 10.1080/15567036.2020.1804489.
- [6] El-Sawaf, I.A., Halawa, M.A., Younes, M.A., Teaima, I.R. Study of the Different Parameters That Influence on the Performance of Water Jet Pump, *Fifteenth Int. Water Technol. Conf. IWTC 15*, 2011, 1–17.
- [7] Zhu, Y., Jiang, P. Experimental and analytical studies on the shock wave length in convergent and convergent–divergent nozzle ejectors, *Energy Conversion and Management*, 88, 2014, 907–14.
- [8] Chen, Z., Jin, X., Shimizu, A., Hihara, E., Dang, C. Effects of the nozzle configuration on solar-powered variable geometry ejectors, *Solar Energy*, 150, 2017, 75–86.
- [9] Thongtip, T., Aphornratana S. An experimental analysis of the impact of primary nozzle geometries on the ejector performance used in R141b ejector. Refrigerator, *Appl. Therm. Eng.*, 110, 2017, 89–101.
- [10] Rao, S.M.V., Jagadeesh G. Novel supersonic nozzles for mixing enhancement in supersonic ejectors, *Appl. Therm. Eng.*, 71, 2014, 62–71.
- [11] Wang, L., Yan, J., Wang, C., Li, X. Numerical study on optimization of ejector primary nozzle geometries, *International Journal of Refrigeration*, 76, 2017, 219–229.
- [12] Hakkaki-Fard, A., Aidoun, Z., Ouzzane, M. A computational methodology for ejector design and performance maximization, *Energy Conversion Management*, 105, 2015, 1291–1302.
- [13] Hwang, J.C., Cho, W., Wu, C., Chiu, K., Lin, C. Numerical and experimental investigation into passive hydrogen recovery scheme using vacuum ejector, *Journal of Power Sources*, 275, 2015, 539–546.
- [14] Wang, X., Xu, S., Xing, C. Numerical and experimental investigation on an ejector designed for an 80 Kw polymer electrolyte membrane fuel cell stack, *Journal of Power Sources*, 415, 2019, 25–32.
- [15] Nikiforow, K., Koski, P., Karimäki, H., Ithonen, J., Alopaeus, V. Designing a hydrogen gas ejector for 5 kW stationary PEMFC system – CFD-modeling and experimental validation, *International Journal of Hydrogen Energy*, 41, 2016, 14952–14970.
- [16] Orozco, W., *Modelo matemático de una bomba chorro para la producción de 8 kPa que permita la destilación de etanol*, MSc. Thesis, Instituto Tecnológico Metropolitano, Medellín, Colombia, 2013.
- [17] Orozco, W., Destilación al vacío de etanol usando bomba chorro, *Tecnológicas*, 25, 2010, 77–96.
- [18] Orozco, W., Palacio, J.A., Patiño, I.D., Zapata, J.S., Hincapié, J.A. Analysis of a Jet Pump Performance under Different Primary Nozzle Positions and Inlet Pressures using two Approaches: One Dimensional Analytical Model and Three Dimensional CFD Simulations, *J. Appl. Comput. Mech.*, 6, 2020, 1228–1244.
- [19] Uyazán, A.M., Gil, I.D., Aguilar, J.L., Rodríguez, G., Caicedo, L.A., Deshidratación del etanol, *Ing e Investig*, 24, 2004, 49–59.
- [20] Bianco, N., Iasiello, M., Mauro, G. M., Busiello, S. Finned heat sinks with phase change materials and metal foams: Pareto optimization to address cost and operation time, *Applied Thermal Engineering*, 197, 2021, 117436
- [21] Bianco, N., Iasiello, M., Mauro, G.M., Pagano, L. Multi-objective optimization of finned metal foam heat sinks: Tradeoff between heat transfer and pressure drop, *Applied Thermal Engineering*, 182, 2021, 116058.
- [22] Li, H., Xu, B., Lu, G., Du, C., Huang, N. Multi-objective optimization of PEM fuel cell by coupled significant variables recognition, surrogate models and a multi-objective genetic algorithm, *Energy Conversion and Management*, 236, 2021, 114–123.
- [23] Chong, D., Hu, M., Chen, W., Wang, J., Liu, J., Yan, J. Experimental and numerical analysis of supersonic air ejector, *Applied Energy*, 130, 2014, 679–684.
- [24] Hosseinzadeh, E., Rokni, M., Jabbari, M., Mortensen, H. Numerical analysis of transport phenomena for designing of ejector in PEM forklift system, *International Journal of Hydrogen Energy*, 39(12), 2014, 6664–6674.
- [25] Mazzelli, F., Little, A.B., Garimella, S., Bartosiewicz, Y. Computational and experimental analysis of supersonic air ejector: Turbulence modeling and assessment of 3D effects, *International Journal of Heat and Fluid Flow*, 56, 2015, 305–316.
- [26] Yin, Y., Fan M., Jiao K., Du Q., Qin Y. Numerical investigation of an ejector for anode recirculation in proton exchange membrane fuel cell system, *Energy Conversion and Management*, 126, 2016, 1106–1117.
- [27] Shah, A., Chughtai, I.R., Inayat, M.H. Experimental and numerical analysis of steam jet pump, *Int. J. Multiph. Flow*, 37, 2011, 1305–1314.
- [28] Song, X-G., Park, J-H., Kim, S-G., Park, Y-C. Performance comparison and erosion prediction of jet pumps by using a numerical method, *Math. Comput. Model.*, 57, 2013, 245–253.
- [29] Yapici, R., Aldas K. Optimization of water jet pumps using numerical simulation, *Proc. Inst. Mech. Eng. Part A J. Power Energy*, 227, 2013, 438–449.
- [30] Zheng, P., Li, B., Qin, J. CFD simulation of two-phase ejector performance influenced by different operation conditions, *Energy*, 155, 2018, 1129–1145.




- [31] Deng, X., Dong, J., Wang, Z., Tu, J. Numerical analysis of an annular water–air jet pump with self-induced oscillation mixing chamber, *Journal of Computational Multiphase Flows*, 9, 2017, 47-53.
- [32] Momeni, H., Domagała, M. CFD simulation of transport solid particles by jet pumps, *Czasopismo Techniczne*, 7, 2016, 185-191.
- [33] Fan, J., Eves, J., Thompson, H.M., Toropov, V.V., Kapur, N., Copley, D., et al. Computational fluid dynamic analysis and design optimization of jet pumps, *Computers and Fluids*, 46, 2011, 212-217.
- [34] Wang, X.-D., Dong, J.-L., Numerical study on the performances of steam-jet vacuum pump at different operating conditions, *Vacuum*, 84, 2010, 1341-1346.
- [35] Wilcox, D. *Turbulence Modeling for CFD*, Third Edition, DCW Industries – California, 2006.
- [36] Launder, B., Spalding, D.B. The Numerical Computation of Turbulent Flow Computer Methods, *Computer Methods in Applied Mechanics and Engineering*, 3(2), 1974, 269-289
- [37] Varga, S., Oliveira, A.C., Ma, X., Omer, S.A., Zhang, W., Riffat, S.B. Experimental and numerical analysis of a variable area ratio steam ejector, *Int. J. Refrig.*, 34, 2011, 1668-1675.
- [38] Rusly, E., Aye, L., Charters, W.W.S., Ooi, A. CFD analysis of ejector in a combined ejector cooling system, *Int. J. Refrig.*, 28, 2005, 1092-1101.
- [39] Sriveerakul, T., Aphornratana, S., Chunnanond, K. Performance prediction of steam ejector using computational fluid dynamics: Part 1. Validation of the CFD result, *Int. J. Therm. Sci.*, 46, 2007, 812-822.
- [40] Huang, B.J., Chang, J.M. Empirical correlation for ejector design, *Int. J. Refrig.*, 22, 1999, 379-388.
- [41] Anaya, A., Gonzalez, E., Pérez, Ma., Robles, T., Pedro, E. Desarrollo de Tecnología de Diseño de Eyectores, *Instituto Mexicano del Petróleo*, 18, 1986, 65-77.
- [42] Manrique, J. A., *Termodinámica*, Oxford University Press, Mexico, 2001.
- [43] Huan, X., Li, M.J., He, Y.L., Tao, W.O. A graphical criterion for working fluid selection and thermodynamic system comparison in waste heat recovery, *Applied Thermal Engineering*, 89, 2015, 772-782.
- [44] Alyssa, J.S., Stacy, M.N. Multi-objective optimization for coupled mechanics-dynamics analyses of composite structures, *Sandia National Laboratories, Livermore*, 73, 2018, 1-21.
- [45] Aldas, K., Yapici, R. Investigation of effects of scale and surface roughness on efficiency of water jet pumps using CFD, *Eng. Appl. Comput. Fluid Mech.*, 8, 2014, 14-25.
- [46] Dong, J., Wang, X., Tu, J. Numerical research about the internal flow of steam-jet vacuum pump: evaluation of turbulence models and determination of the shock-mixing layer, *Phys. Procedia*, 32, 2012, 614-622.
- [47] Masud, J., Imran, M. *Turbulence Modeling for Realistic Computation of Internal Flow in Liquid Ejector Pumps*, 54th AIAA Aerosp. Sci. Meet., Reston, Virginia: American Institute of Aeronautics and Astronautics, 2016.
- [48] Maharana, P.S. *Efficient Multi-site Statistical Downscaling Model for Climate Change*, Ph.D. Thesis, Motilal Nehru National institute of Technology Allahabad Prayagraj-211004, India, 2018.
- [49] Cengel, Y. *Mecánica de fluidos*, Mc Graw Hill – México, 2006.

ORCID iD

William Orozco Murillo  <https://orcid.org/0000-0003-4115-0286>

Iván D. Patiño Arcila  <https://orcid.org/0000-0002-2876-8930>

José A. Palacio-Fernández  <https://orcid.org/0000-0002-9207-7077>



© 2022 Shahid Chamran University of Ahvaz, Ahvaz, Iran. This article is an open access article distributed under the terms and conditions of the Creative Commons Attribution-Noncommercial 4.0 International (CC BY-NC 4.0 license) (<http://creativecommons.org/licenses/by-nc/4.0/>).

How to cite this article: Murillo W.O., Patiño Arcila I.D., Palacio-Fernández J.A. Geometric Optimization of Jet Pump Used in Vacuum Distillation Applications under Different Operating Conditions using Genetic-algorithm Methods, *J. Appl. Comput. Mech.*, 8(1), 2022, 340-358. <https://doi.org/10.22055/JACM>

Publisher's Note Shahid Chamran University of Ahvaz remains neutral with regard to jurisdictional claims in published maps and institutional affiliations.

